

Global Simulations of Protoplanetary Disk Outflows with Coupled Non-ideal Magnetohydrodynamics and Consistent Thermochemistry

LILE WANG^{1,2}, XUE-NING BAI³, AND JEREMY GOODMAN¹

ABSTRACT

Magnetized winds may be important in dispersing protoplanetary disks and influencing planet formation. We carry out global full magnetohydrodynamic simulations in axisymmetry, coupled with ray-tracing radiative transfer, consistent thermochemistry, and non-ideal MHD diffusivities. Magnetized models lacking EUV photons ($h\nu > 13.6$ eV) feature warm molecular outflows that have typical poloidal speeds $\gtrsim 4$ km s⁻¹. When the magnetization is sufficient to drive accretion rates $\sim 10^{-8} M_{\odot}$ yr⁻¹, the wind mass-loss rate is comparable. Such outflows are driven not centrifugally but by the pressure of toroidal magnetic fields produced by bending the poloidal field. Both the accretion and outflow rates increase with the poloidal field energy density, the former almost linearly. The mass-loss rate is also strongly affected by ionization due to UV and X-ray radiation near the wind base. Adding EUV irradiation to the system heats, ionizes, and accelerates the part of the outflow nearest the symmetry axis, but reduces the overall mass-loss rate by exerting pressure on the wind base. Most of our models are non-turbulent, but some with reduced dust abundance and therefore higher ionization fractions exhibit magnetorotational instabilities near the base of the wind.

Keywords: accretion, accretion disks — magnetohydrodynamics (MHD) — planets and satellites: formation — circumstellar matter — method: numerical

1. INTRODUCTION

Protoplanetary disks (PPDs hereafter) are the birthplaces of planets. During their $\sim 10^6 - 10^7$ yr lifespans, PPDs are believed to disperse in three ways: (1) by forming planets, (2) by accreting onto central protostar, and (3) by outflowing in winds. The latter two processes compete with the first, limiting the time and mass available for planet formation.

Absent magnetic fields, PPD winds must be launched by photoevaporation. High energy photons heat up the gas by photoionization/photodissociation, depositing energy into the gas and unbinding it from the star.

Pioneering theoretical studies of disk photoevaporation simplified this complex problem in complementary ways. Gorti & Hollenbach (2008, 2009) grafted analytic Parker winds onto hydrostatic disk models with relatively detailed thermochemistry. Alexander et al. (2006a,b) performed hydrodynamic simulations with minimal chemistry and thermodynamics. Owen

et al. (2010) took a similar hydrodynamic approach, using an interpolation table for gas temperature as a function of ionization parameter. Recently Wang & Goodman (2017a) (WG17 hereafter) conducted hydrodynamic simulations coupled with radiation and consistent thermochemistry. They found that photoevaporative mass loss is driven mainly by EUV and Lyman-Werner FUV photons rather than higher-energy radiation. Nakatani et al. (2018) reached similar conclusions by similar methods and explored the influence of gas metallicity.

Photoevaporative winds without magnetic fields carry off only their Keplerian share of angular momentum, and are not directly relevant to disk accretion. Other processes must be invoked to explain disk accretion. A magnetized wind, however, may exert torque on the disk, thereby linking accretion to outflow. This fact has recently been realized to be essential as viscous/turbulent accretion via the magnetorotational instability (MRI, Balbus & Hawley 1998) or other hydrodynamic instabilities is generally found to be insufficient under PPD conditions (e.g., Bai & Stone 2013; Bai 2013; Simon et al. 2013b,a; see Turner et al. 2014 for a review).

As is clarified in Bai (2017, hereafter B17), magnetized winds can be divided into two types: (1) magnetocentrifugal winds, whose poloidal fields are strong

¹ Princeton University Observatory, Princeton, NJ 08544

² Center for Computational Astrophysics, Flatiron Institute, New York, NY 10010; lwang@flatironinstitute.org

³ Institute for Advanced Study, Tsinghua University, Beijing 100084, China; xbai@tsinghua.edu.cn

enough to enforce corotation near the wind base, driving an outflow centrifugally; (2) magneto-thermal winds driven by the gradient of total pressure, in particular the energy density in toroidal magnetic fields. Modeling of global wind kinematics suggests that the second type prevails in PPDs (Bai et al. 2016; Bai 2016), but a complete treatment requires global simulations with consistent microphysics.

The co-evolution of radiation, thermochemistry and non-ideal MHD in global disk models could be prohibitively time-consuming if medium or large chemical networks were applied without proper optimization. MHD simulations to date have simplified the treatment of microphysics. Most recently, global simulations have been conducted using 2.5-dimensional axisymmetric full MHD simulations with non-ideal MHD effects, evaluating magnetic diffusivities by a pre-calculated interpolation table, and calculating thermodynamics via a simple relaxation-time recipe with temperature depending on spatial location (Bai 2017).

Here we report full axisymmetric MHD simulations coupled with radiation and thermochemistry: at every time step, in every spatial zone throughout the simulation domain, a moderate-scale chemical network (28 species, ~ 160 reactions) is evolved. The network contains species and reactions that are important for the temperature and ionization of the gas, and hence for the dynamics of the flow, but omits some trace species that are important as observational diagnostics (e.g. neon); these species will be included in post-processing analyses to be reported in subsequent publications. In contrast to simulations using pre-calculated interpolation tables, our approach offers a consistent treatment of regions where thermal or chemical timescales are comparable to flow timescales.

This paper is structured as follows. §2 briefly summarizes the numerical methods and physical recipes we adopt for carrying out and analyzing our simulations. Some details are further elaborated in the Appendices. §3 describes the setup and parameter choices for our fiducial simulation and explains the underlying physics, while §4 presents and discusses the main results for this model. §5 explores the parameter space to understand the impact of different physical assumptions. In §6 we compare our results to those in B17 and WG17, and discuss prospective observational tests. A summary of our main results and conclusions is given in §7.

2. METHOD

Our computational methods are summarized in this section. We describe first the scheme for magnetohydrodynamics (MHD). Then we discuss our methods for ra-

diative transfer, thermochemistry, and non-ideal MHD effects, the former being two largely the same as in WG17.

2.1. Magnetohydrodynamics

We use the grid-based higher-order Godunov MHD code **Athena++** (White et al. 2016; J. Stone et al., in preparation) in spherical-polar coordinates (r, θ, ϕ) . We assume axisymmetry (and hence 2D), and with reflective reflection symmetry across the equatorial ($\theta = \pi/2$) plane. All dependence on ϕ is neglected, but v_ϕ and B_ϕ are still included in our simulations. For convenience, we also occasionally use cylindrical coordinates (R, z) , defined as $R \equiv r \sin \theta$, and $z \equiv r \cos \theta$. The HLLD Riemann solver and piecewise linear reconstruction are employed in all our simulations.

Athena++ solves the MHD equations in conservative form, and therefore conserves mass, energy, (angular) momentum and magnetic flux to machine precision. The equations read

$$\begin{aligned} \partial_t \rho + \nabla \cdot (\rho \mathbf{v}) &= 0 ; \\ \partial_t (\rho \mathbf{v}) + \nabla \cdot \left(\rho \mathbf{v} \mathbf{v} - \frac{\mathbf{B} \mathbf{B}}{4\pi} + P_{\text{tot}} \mathbf{I} \right) &= -\nabla \Phi ; \\ \partial_t \mathbf{B} &= \nabla \times (\mathbf{v} \times \mathbf{B} - c \mathbf{E}') ; \\ \partial_t \epsilon + \nabla \cdot \left[(\epsilon + P_{\text{tot}}) \mathbf{v} - \frac{(\mathbf{B} \cdot \mathbf{v}) \mathbf{B}}{4\pi} + \mathbf{S}' \right] &= 0 , \end{aligned} \quad (1)$$

where ρ , \mathbf{v} and p are the gas density, velocity and gas thermal pressure respectively, \mathbf{B} is the magnetic field, $P_{\text{tot}} \equiv p + B^2/(8\pi)$ is the total pressure, $\epsilon \equiv p/(\gamma - 1) + \rho(v^2/2 + \Phi) + B^2/(8\pi)$ is the total energy density (γ is the adiabatic index), Φ is the gravitational potential, and \mathbf{I} is the identity tensor. Non-adiabatic processes that affect gas energy are calculated separately in an operator-splitting manner (see §2.2).

As a general equation of state (with variable γ) is not yet implemented in the current version of **Athena++** we adopt an ideal equation of state with constant $\gamma = 5/3$. Admittedly γ should increase from $\gamma = 1.4$ in the molecular disk to $\gamma = 5/3$ in regions where molecules are dissociated. We address this issue further in §5.

Non-ideal MHD entails an electric field in the local fluid rest frame,

$$\mathbf{E}' = \frac{4\pi}{c^2} (\eta_O \mathbf{J} + \eta_H \mathbf{J} \times \mathbf{b} + \eta_A \mathbf{J}_\perp) , \quad (2)$$

where $\mathbf{b} \equiv \mathbf{B}/B$ is a unit vector along the local direction of magnetic field, $\mathbf{J} = c \nabla \times \mathbf{B}/4\pi$ is the current density, and $\mathbf{J}_\perp \equiv \mathbf{b} \times (\mathbf{J} \times \mathbf{b})$ is the component of \mathbf{J} perpendicular to the local magnetic field. The Poynting flux associated with \mathbf{E}' reads $\mathbf{S}' = c \mathbf{E}' \times \mathbf{B}/(4\pi)$. In this

paper, we ($\eta_{\text{H}} = 0$). The Ohmic (η_{O}) and ambipolar (η_{A}) diffusivities are calculated using the thermochemical network described in §2.2.

2.2. Radiative Transfer and Thermochemistry

Radiation and thermochemical reactions are important for the temperature, ionization fraction, and molecular or atomic composition of the gas. We solve the coupled thermochemistry-radiation problem in conjunction with the MHD equations via operator splitting (see also WG17, L. Wang 2018, in preparation).

UV and X-ray photons are emitted isotropically from a point source at the origin ($r = 0$). The luminosity of each ray is adjusted according to photoreactions and absorptions as it propagates through the grid cells. Because individual cells are sometimes optically thick, we calculate the local effective flux at photon energy $h\nu$ as

$$F_{\text{eff}}(h\nu) = \sum_{\{i \text{ in cell}\}} F_i(h\nu) \left\{ \frac{1 - \exp[-\delta l_i / \lambda(h\nu)]}{\delta l_i / \lambda(h\nu)} \right\}, \quad (3)$$

where $F_i(h\nu)$ is the flux of the i th ray as it enters the cell, δl_i is the chord length of the ray across the cell, and $\lambda(h\nu)$ is the mean free path of photon absorption at energy $h\nu$. For each $h\nu$, $\lambda(h\nu)$ is calculated by collecting all absorption mechanisms, and is updated as the abundances of species evolve. As self-/cross-shielding effects are important especially for some FUV photoreactions, the calculation of $\lambda(h\nu)$ becomes trickier than for other photon energies; we refer the reader to Appendix A.2 for more details.

In this work we use four discrete energy bins to represent four important bands of photon energy: $h\nu = 7$ eV (“soft FUV” hereafter, for FUV photons that do not interact appreciably with hydrogen molecules), 12 eV for Lyman-Werner (“LW”) band photons, 25 eV for EUV photons, and 3 keV for X-ray photons (rather than 1 keV as in WG17). For FUV and EUV, absorption processes overwhelm scattering (Verner & Yakovlev 1995; Verner et al. 1996; Draine 2011). However, scattering may allow X-ray and Ly α photons to penetrate more deeply into the disk, in part by deflecting radial into latitudinal propagation. For X-ray photons, we adopt the recipes summarized in Appendix A.1, together with recipes for ionization by cosmic rays and radioactive decays. Ly α photons do not affect the most abundant chemical species (H_2 , H, He, CO), yet could still affect the thermal state by photodissociating H_2O and OH, and by photoelectric emission from dust grains. However, via the same approach as WG17, we have confirmed that Ly α photons have only secondary importance compared to UV and X-ray photons in both re-

spects¹. Therefore, in this paper, we focus on radial ray tracing for the radiative transfer problem.

Optical and infrared radiation from the central protostar is not directly relevant to the thermal structure of the outflow or the ionization structure of the disk (except within ~ 0.1 au of the star). Nevertheless, the temperature profile in the regions unreachable by high-energy photons is affected by the diffuse radiation in these two bands, which maintains the dust temperature and therefore also the gas temperature by thermal accommodation on grains. Following WG17, we take the following approach. We set the dust temperature following the simple model of Chiang & Goldreich (1997), using the following equation,

$$4\sigma_{\text{SB}}T_{\text{dust}}^4\sigma_{\text{dust}}q(T_{\text{dust}}) = \max \left[4\sigma_{\text{SB}}T_{\text{ah}}^4(R)\sigma_{\text{dust}}q(T_{\text{dust}}), \sum_{h\nu} F_{\text{eff}}(h\nu)\sigma(h\nu) \right], \quad (4)$$

where T_{ah} is the desired temperature as a function of cylindrical radius R (e.g. Chiang & Goldreich 1997, figure 4),

$$T_{\text{ah}} \simeq 280 \text{ K} \times (R/\text{au})^{-0.5}. \quad (5)$$

Also, σ_{dust} is the geometric dust-grain cross section, $q(T_{\text{dust}})$ is the Planck-averaged emissivity (see also equation (24.16) in Draine 2011), $F_{\text{eff}}(h\nu)$ is the local high-energy radiation flux in photon-energy bin $h\nu$, and $\sigma(h\nu)$ is the effective absorption cross section. In every timestep, T_{dust} is first calculated by solving eq. (4). The gas temperature is then related to the dust temperature via the dust-gas heat accommodation term (Goldsmith 2001; Draine 2011),

$$\Gamma_{\text{dust}} = -k_{\text{B}}(T - T_{\text{dust}})\sigma_{\text{dust}} \sum_{\text{sp}} n_{\text{sp}} \left(\frac{8k_{\text{B}}T}{\pi m_{\text{sp}}} \right)^{1/2}, \quad (6)$$

where the subscripts “sp” range over species. Note that Γ_{dust} is negative when the gas is hotter than the dust. When other heating/cooling processes are weak, these prescriptions will stabilize gas temperature at the dust temperature (5).

¹ Following the scheme in WG17 (based on the method described by Bethell & Bergin (2011)), we have applied our Ly α Monte-Carlo radiation code to our fiducial model. We assume that the luminosity in Ly α is the same as that of the 7 eV soft FUV energy band. We find that (a) in the intermediate layer, the photodissociation rate by Ly α is at most a tenth of that by 7 eV photons; (b) the ionization rate by Ly α is $\lesssim 10^{-1}$ of that by direct or scattered X-ray photons everywhere below the wind base.

Advection of chemicals is calculated with special methods (L. Wang 2018, in preparation) so that consistency of chemical elements and species fluxes in every timestep of MHD evolution is ensured. Advected abundance of chemicals and internal energy density is then used as the input to the thermochemical calculations for the current step. The following coupled set of ordinary differential equations (ODEs) is solved (in which the Einstein summation convention applies):

$$\begin{aligned} \frac{dn^i}{dt} &= \mathcal{A}_{jk}^i n^j n^k + \mathcal{B}_j^i n^j ; \\ \frac{d\epsilon}{dt} &= \Gamma - \Lambda ; \end{aligned} \quad (7)$$

in which the terms $\{\mathcal{A}_{jk}^i\}$ describe two-body reactions, those in $\{\mathcal{B}_j^i\}$ represent photoionization, photodissociation, and spontaneous decays, and Γ and Λ represent all non-adiabatic heating and cooling rates per unit volume, respectively. Dust-gas heat accommodation (eq. 6) is included in the Γ term.

Because the ODEs (7) are usually stiff, we use a multi-step implicit method to solve them. By implementing the thermochemical calculations on GPUs, we have reduced the (wall-clock) time spent on them so that it is comparable to that spent by the CPUs on the MHD (L. Wang 2018, in preparation).

The set of chemical species and reactions broadly follows WG17, with some updates so that, based on our tests, the ionization in the intermediately ionized regions can be calculated with relatively good accuracy while the cost of computation is minimized. These 28 species are: e^- (free electrons), H^+ , H , H_2 , H_2^* [using the $v = 6$ vibrational state as a proxy for H_2 in all excited states, see Tielens & Hollenbach 1985, (TH85), WG17], He , He^+ , O , O^+ , OH , OH^+ , H_2O , C , C^+ , CO , HCO^+ , CH^+ , S , S^+ , HS^+ , Si , Si^+ , SiO , SiO^+ , $SiOH^+$, Gr , Gr^+ , Gr^- . Here Gr and Gr^\pm denote neutral and singly-charged dust grains, respectively.

The thermochemical mechanisms involved and pertinent references are summarized below:

- “Standard” two-body interactions in the UMIST database (McElroy et al. 2013; the photochemical reactions therein are excluded as they are not suitable for our radiation fields).
- Photoionization/photodissociation of atoms and molecules (Verner & Yakovlev 1995; Verner et al. 1996 for ionization; TH85 for H_2 dissociation; Visser et al. 2009 for CO dissociation; Ádámkovics et al. (2014) for OH/H_2O dissociation); some photoionization/photodissociation processes are subject to self-/cross-shielding (Heays et al. (2017); see also Appendix A.2).

- Dust-assisted molecule formation (Bai & Goodman 2009; Ádámkovics et al. 2014) and recombination (Draine & Sutin 1987; Weingartner & Draine 2001; see also the compilation in Ilgner & Nelson 2006); photoelectric emission by dust (Li & Draine 2001; Weingartner & Draine 2001); dust-gas heat accommodation (eq. 6). For simplicity, we follow WG17 and use single-sized dust grains with $r_{\text{dust}} = 5 \text{ \AA}$, which serve as a proxy for dust grains of all sizes in terms of their impact on thermochemistry and ionization.
- Cooling by atomic/ionic transitions (Tielens & Hollenbach 1985, using an escape-probability formalism as described in Kwan & Krolik 1981); and by ro-vibrational transitions of molecules (Neufeld & Kaufman 1993; Omukai et al. 2010).

Our thermochemical network is tuned to capture the important reactions relevant to regions near the wind base and in the wind proper. It is less accurate in the denser regions near the midplane, particularly with regard to ionization levels. However, this issue does not undermine our analyses in this paper: as shown in what follows (e.g. §4.1.4), the accretion rate is determined by magnetic stresses near the wind base instead of those in the midplane.

2.3. Non-ideal MHD Diffusivities

Non-ideal MHD diffusivities are determined by the abundances of charge carriers, which are computed as part of our thermochemical network. The general expressions for the three diffusivities read (e.g. Wardle 2007; Bai 2011b),

$$\begin{aligned} \eta_O &= \frac{c^2}{4\pi} \left(\frac{1}{\sigma_O} \right) , \quad \eta_H = \frac{c^2}{4\pi} \left(\frac{\sigma_H}{\sigma_H^2 + \sigma_P^2} \right) \\ \eta_A &= \frac{c^2}{4\pi} \left(\frac{\sigma_P}{\sigma_H^2 + \sigma_P^2} \right) - \eta_O , \end{aligned} \quad (8)$$

Here σ_O , σ_H and σ_P are Ohmic, Hall, and Pederson conductivities. If $Z_j e$ is the charge and n_j the number density of the j^{th} charged species, then

$$\begin{aligned} \sigma_O &= \frac{ec}{B} \sum_j n_j Z_j \beta_j , \quad \sigma_H = \frac{ec}{B} \sum_j \frac{n_j Z_j}{1 + \beta_j^2} , \\ \sigma_P &= \frac{ec}{B} \sum_j \frac{n_j Z_j \beta_j}{1 + \beta_j^2} , \end{aligned} \quad (9)$$

in which the Hall parameter β_j is the ratio of the gyrofrequency to the collision rate with neutrals,

$$\beta_j = \frac{Z_j e B}{m_j c} \frac{1}{\gamma_j \rho} ; \quad \gamma \equiv \frac{\langle \sigma v \rangle_j}{\langle m \rangle_n + m_j} , \quad (10)$$

where m_j is the charged species' molecular mass, $\langle m \rangle_n$ is the mean molecular mass of the neutrals, and $\langle \sigma v \rangle_j$ is the rate of collisional momentum transfer between the j th species and the neutrals, given by (e.g. [Draine 2011](#); [Bai 2011a](#), $T_2 \equiv (T/10^2 \text{ K})$),

$$\begin{aligned} \langle \sigma v \rangle_e &\simeq 8.3 \times 10^{-9} \text{ cm}^3 \text{ s}^{-1} \times \max\{T_2^{1/2}, 1\}, \\ \langle \sigma v \rangle_i &\simeq 2.0 \times 10^{-9} \text{ cm}^3 \text{ s}^{-1} \times \left(\frac{\langle m \rangle_n m_i / m_p}{\langle m \rangle_n + m_i} \right)^{-1/2}, \end{aligned} \quad (11)$$

for electrons and ions, respectively. As our dust grains are tiny, their collisional momentum transfer rate $\langle \sigma v \rangle_g$ can be approximated by the rate for ions, but the actual grain mass is used for m_j in eq. (10). Although all three diffusivities are calculated, η_H is not actually used in this paper, as the Hall effect is neglected.

We have tested the diffusivities calculated from our thermochemical network under the same magnetic, thermal, and radiation conditions as those of Figure 5 in [Xu & Bai \(2016\)](#), using a hydrostatic grid and prescribed temperature. The error in the Elsasser numbers Am and Λ_{Ohmic} is $\lesssim 10\%$ at higher altitudes ($z/H \gtrsim 2 h_{\text{mid}}$, where h_{mid} is the gaussian scale height at the equatorial plane), and no more than one order of magnitude in the mid-plane regions.

The ambipolar diffusivity η_A computed in this way is very large in two regions that do not much concern us in this paper. First, near the polar axis, the density is very low, the gas is highly ionized ($x_e \gtrsim 10^{-1}$), and the one-fluid treatment of magnetic diffusivity simply fails. Second, near the midplane the ionization is extremely weak ($x_e \lesssim 10^{-11}$). To avoid the prohibitively small time steps that would otherwise be required to evolve the diffusive terms stably, we cap η_A at $\eta_{A,\text{cap}} = [10c_{s,\text{mid}}h_{\text{mid}}]_{r=r_{\text{in}}}$, where $c_{s,\text{mid}}$ denotes the adiabatic sound speed at the equatorial plane (similar schemes capping diffusivity were also adopted in e.g. [Bai & Stone 2013](#); [Gressel et al. 2015](#), B17). This cap does not harm our simulations because (1) in highly ionized regions, the plasma is already in the ideal MHD regime; and (2), in regions with very weak ionization, the magnetic diffusivity is dominated by Ohmic resistivity. An identical cap is also applied to η_O ; in simulations throughout this paper, however, this η_O cap is never reached.

2.4. Diagnostics of MHD Wind Models

This subsection briefly discusses the major diagnostics that we have used to analyze our simulations.

2.4.1. Magnetic diffusivities

As the Hall effect is neglected, non-ideal MHD effects are characterized by these two dimensionless Elsasser numbers,

$$\Lambda_{\text{Ohmic}} \equiv \frac{v_A^2}{\eta_O \Omega_K}, \quad \text{Am} \equiv \frac{v_A^2}{\eta_A \Omega_K}, \quad (12)$$

where $v_A = (B^2/4\pi\rho)^{1/2}$ is the Alfvén speed, and $\Omega_K = \sqrt{GM_*/r^3}$ is the local Keplerian angular frequency. Magnetic diffusion is considered to be strong if either Elsasser number is $\lesssim 1$. In general, $\Lambda_{\text{Ohmic}} \lesssim 1$ is sufficient to suppress MRI (e.g. [Turner et al. 2007](#); [Ilgner & Nelson 2008](#)). ([Bai & Stone 2011](#)) found that the plasma $\beta \equiv 8\pi p/B^2 \lesssim \beta_{\text{min}}(\text{Am})$ is also able to damp or suppress MRI, where

$$\beta_{\text{min}}(\text{Am}) = \left[\left(\frac{50}{\text{Am}^{1.2}} \right)^2 + \left(\frac{8}{\text{Am}^{0.3} + 1} \right)^2 \right]^{1/2}. \quad (13)$$

2.4.2. Wind kinematics and dynamics

Following B17, we locate the wind base at the FUV front, where the radial absorption optical depth in the soft FUV band is unity. The mechanisms that launch the outflow near the wind base are of interest. Following [Bai et al. \(2016\)](#) and B17, we project the forces acting on fluid elements onto the local poloidal magnetic field and decompose them into three terms,

$$\begin{aligned} \left(\frac{dv_p}{dt} \right)_s &= f_{\text{gas}} + f_{\text{ine}} + f_{\text{mag}}; \\ f_{\text{gas}} &\equiv -\frac{dp}{ds}; \quad f_{\text{ine}} \equiv \frac{v_\phi^2}{R} \frac{dR}{ds} - \frac{d\Phi}{ds}; \\ f_{\text{mag}} &= -\frac{B_\phi}{4\pi\rho R} \frac{d(RB_\phi)}{ds}, \end{aligned} \quad (14)$$

where, along a field line, f_{gas} and f_{mag} are accelerations due to gas and magnetic pressure gradients respectively, and f_{ine} is the net inertial acceleration (combining centrifugal and gravitational forces).

The wind mass loss rate \dot{M}_{wind} is an important diagnostic of disk dispersal. We characterize \dot{M}_{wind} by the local wind mass loss rate per logarithmic radius,

$$\frac{d\dot{M}_{\text{wind}}}{d \ln R} = 4\pi R^2 \langle \rho v_z \rangle|_{z_{\text{wb}}}. \quad (15)$$

We write \dot{M}_{wind} for the integral of this between our radial boundaries.

Following B17, we use the following quantities that would be conserved along magnetic field lines in steady

winds in the ideal MHD regime,

$$\begin{aligned} k &\equiv \frac{4\pi\rho v_p}{B_p}, \quad \omega \equiv \frac{v_\phi}{R} - \frac{kB_\phi}{4\pi\rho R}, \quad l \equiv v_\phi R - \frac{RB_\phi}{k}; \\ k_0 &\equiv \frac{4\pi\rho_{\text{mid}}v_K}{B_{z0}}, \quad \omega_0 \equiv \Omega_K(R_{\text{wb}}), \\ l_0 &\equiv \Omega_K(R_{\text{wb}})R_{\text{wb}}^2. \end{aligned} \quad (16)$$

Here the subscript “p” denotes a poloidal component, v_K is the Keplerian speed, and R_{wb} is the cylindrical radius of the wind base along the same field line. The symbols k , ω and l stand for poloidal mass flux per magnetic flux, angular velocity of the magnetic line, and specific angular momentum, while k_0 , ω_0 and l_0 are reference values defined at or near the wind base.

2.4.3. Wind versus accretion: Angular momentum transfer

A key concept of all steady magnetized wind models is the poloidal Alfvén radius R_A , which is defined as the cylindrical radius of the point along the field line where the poloidal velocity v_p equals the poloidal Alfvén velocity $v_{A,p} \equiv B_p/(4\pi\rho)^{1/2}$. At R_A , the accretion and outflow rates are related in steady state by (e.g. [Ferreira & Pelletier 1995](#); [Bai et al. 2016](#))

$$\xi \equiv \left(\frac{1}{\dot{M}_{\text{acc}}} \right) \left(\frac{d\dot{M}_{\text{wind}}}{d \ln R} \right) = \frac{1}{2} \frac{1}{(R_A/R_{\text{wb}})^2 - 1}. \quad (17)$$

The quantity (R_A/R_{wb}) is often referred to as the “magnetic lever arm,” and ξ is called the “ejection index.”

In a steady or statistically states where magnetic stresses dominate the transport of angular momentum,

$$\frac{\dot{M}_{\text{acc}}v_K}{4\pi} = \frac{\partial}{\partial R} \left(R^2 \int_{-z_{\text{wb}}}^{z_{\text{wb}}} dz \langle T_{R\phi} \rangle_{t,\phi} \right) + R^2 \langle T_{z\phi} \rangle_{t,\phi} \Big|_{-z_{\text{wb}}}^{z_{\text{wb}}}. \quad (18)$$

Here $\dot{M}_{\text{acc}} \equiv -2\pi R \int_{-z_{\text{wb}}}^{z_{\text{wb}}} dz \rho v_R$ is the radial accretion rate at radius R , $T_{ij} \equiv -B_i B_j / (4\pi)$ are components of the Maxwell stress tensor (not to be confused with gas temperature), and angle brackets stand for temporal and azimuthal averaging. Eq. (18) assumes that azimuthal velocities are close to the local Keplerian speed. The first term in eq. (18) resembles a radial viscous stress and can be characterized by the classic dimensionless α parameter ([Shakura & Sunyaev 1973](#)),

$$\alpha \equiv \left[\int_{-z_{\text{wb}}}^{z_{\text{wb}}} dz p \right]^{-1} \times \int_{-z_{\text{wb}}}^{z_{\text{wb}}} dz \langle T_{R\phi} \rangle. \quad (19)$$

The second term in eq. (18) represents the vertical component of angular momentum transfer. Comparison of these two terms reveals which type of angular momentum transport mechanism dominates in the disk.

2.4.4. Energy budget

Analyzing the energy budget of the wind helps us to compare various factors that contribute to wind dynamics and thermodynamics. In steady states ($\partial_t \rightarrow 0$) the rates of change of the gas internal and mechanical energy read, respectively (see also [Balbus & Hawley 1998](#)),

$$\begin{aligned} \nabla \cdot F_{\text{int}} &= -p \nabla \cdot \mathbf{v} + \Gamma - \Lambda + (\Gamma_A + \Gamma_O); \\ \nabla \cdot F_{\text{mech}} &= p \nabla \cdot \mathbf{v} + \nabla \cdot F_{\text{mag}} - (\Gamma_A + \Gamma_O), \end{aligned} \quad (20)$$

where Γ and Λ are thermal chemical heating and cooling rates of the gas (eq. 7), and

$$\Gamma_A \equiv \frac{4\pi\eta_A}{c^2} \mathbf{J}_\perp^2, \quad \Gamma_O \equiv \frac{4\pi\eta_O}{c^2} \mathbf{J}^2, \quad (21)$$

are the heating rates due to ambipolar diffusion and Ohmic resistivity, and

$$F_{\text{int}} \equiv \frac{p\mathbf{v}}{\gamma - 1}, \quad F_{\text{mech}} \equiv \left(\frac{\rho v^2}{2} + \rho\Phi + p \right) \mathbf{v}, \quad (22)$$

are the fluxes in internal and mechanical energy of the gas, and

$$F_{\text{mag}} \equiv -\frac{\mathbf{B} \times (\mathbf{v} \times \mathbf{B})}{4\pi} - \mathbf{S}', \quad (23)$$

denotes the dynamic flux of electromagnetic fields. Decomposing $\nabla \cdot F_{\text{int}}$ and $\nabla \cdot F_{\text{mech}}$ by eq. (20) will shed light onto the energetic evolution of fluids at different spacial locations.

In addition to the local energy balance (eq. 20), another flavor of energy budget analysis involves the wind as a whole. Integrating the combination of eqs. (20) on the volume of a steady wind, we obtain,

$$\dot{E}_{\text{int}} + \dot{E}_{\text{mech}} + \dot{E}_{\text{na}} + \dot{E}_{\text{mag}} = 0. \quad (24)$$

Our sign convention is that $\dot{E}_X > 0$ means that energy of type X leaves the wind region (for example, $\dot{E}_{\text{cool}} \geq 0$ in the following eq 27). Using the divergence theorem, the internal term quantifies the net power brought into the wind by internal energy flux then reads,

$$\dot{E}_{\text{int}} \equiv \oint_{\partial(\text{wind})} d\hat{S} \cdot F_{\text{int}}. \quad (25)$$

Here the subscript “ $\partial(\text{wind})$ ” denotes the boundaries of the wind region, and $d\hat{S}$ is the area integration measure with outward-pointing normal. The mechanical term is decomposed into the net power brought by fluxes in kinetic (further decomposed into toroidal and poloidal

components), gravitational and pdV energy,

$$\begin{aligned}\dot{E}_{\text{mech}} &\equiv \dot{E}_{\text{k,p}} + \dot{E}_{\text{k},\phi} + \dot{E}_{\text{grav}} + \dot{E}_{pdV} ; \\ \dot{E}_{\text{k,p};\phi} &\equiv \oint_{\partial(\text{wind})} d\hat{S} \cdot \mathbf{v} \left(\frac{\rho v_{\text{p};\phi}^2}{2} \right) , \\ \dot{E}_{\text{grav}} &\equiv \oint_{\partial(\text{wind})} d\hat{S} \cdot \mathbf{v} \rho \Phi , \quad \dot{E}_{pdV} \equiv \oint_{\partial(\text{wind})} d\hat{S} \cdot \mathbf{v} p .\end{aligned}\quad (26)$$

The non-adiabatic term integrates contributions of thermochemical processes over the wind volume,

$$\dot{E}_{\text{na}} \equiv \dot{E}_{\text{heat}} + \dot{E}_{\text{cool}} \equiv \int_{\text{wind}} dV (-\Gamma) + \int_{\text{wind}} dV \Lambda . \quad (27)$$

The power in electromagnetic fields sums up the contributions of magnetic stress, magnetic energy flux and Poynting flux,

$$\begin{aligned}\dot{E}_{\text{mag}} &\equiv \dot{E}_{\mathbf{S}'} + \dot{E}_{\mathbf{B}} + \dot{E}_{\text{stress}} ; \\ \dot{E}_{\mathbf{S}'} &\equiv \oint_{\partial(\text{wind})} d\hat{S} \cdot \mathbf{S}' , \quad \dot{E}_{\mathbf{B}} \equiv \oint_{\partial(\text{wind})} d\hat{S} \cdot \frac{\mathbf{v} B^2}{4\pi} , \\ \dot{E}_{\text{stress}} &= \oint_{\partial(\text{wind})} d\hat{S} \cdot \left[-\frac{(\mathbf{B} \cdot \mathbf{v}) \mathbf{B}}{4\pi} \right] .\end{aligned}\quad (28)$$

We notice that the power of magnetic stress term is usually dominated by the power at which magnetic stress does work on the wind base,

$$\dot{E}_{\text{stress}} \simeq - \int_{\text{wb}} dS \frac{B_z B_\phi v_\phi}{4\pi} . \quad (29)$$

3. FIDUCIAL MODEL SETUP

3.1. Geometry of the Simulation Domain

The simulations are axisymmetric (independent of ϕ), spanning the radial range $(r/\text{au}) \in [1, 100]$ and colatitude range $\theta \in [0.035, \pi/2]$. Reflection symmetry about the equatorial plane (midplane: $\theta = \pi/2$) is imposed; all global quantities (e.g. wind mass loss rate, accretion rate) include the contributions from both sides of the plane. The standard resolution is 384 radial by 128 latitudinal. The radial zones are spaced logarithmically. The latitudinal zones have grid spacing $\Delta\theta$ decreasing in geometric progression from pole to midplane, so that $\Delta\theta$ at the midplane is 1/6 as large as near the pole. As the mid-plane scale height is roughly $h_{\text{mid}} \sim 0.05 - 0.10R$, this grid geometry gives 20-25 latitudinal zones per h_{mid} at the disk mid-plane.

3.2. Central Protostar and Radiation Sources

The gravitational field is provided by a $1 M_\odot$ point source located at the origin. The radiation sources are co-centered at the origin and radiate rays isotropically into the simulation domain. In order to approximate attenuation of radiation from the source interior to the inner boundary, we adopt a “pre-absorption” recipe that is elaborated in Appendix A.3. This avoids instabilities caused by unphysically high ionization rates due to unattenuated rays reaching the mid-plane near the inner boundary. In the fiducial model, the EUV bin is *turned off*, for better comparison with B17. The number of photons radiated in soft FUV and LW FUV bands per unit time follows a 9000 K black body integrated over the photon energy range $6 \text{ eV} < h\nu < 13.6 \text{ eV}$, with total luminosity $L_{\text{FUV}} = 10^{31.7} \text{ erg s}^{-1}$ (see also Gorti & Hollenbach 2009, WG17). The X-ray luminosity is $L_X = 10^{30} \text{ erg s}^{-1}$, matching B17 but approximately half of the value in WG17.

3.3. Initial and Boundary Conditions

The initial disk density and temperature profiles follow the steady state solution in Nelson et al. (2013): we set the mid-plane density as $\rho = 2.38 \times 10^{14} m_p \text{ cm}^{-3} (R/\text{au})^{-q_\rho}$ and temperature $T = 280 \text{ K} (R/\text{au})^{-q_T}$, with the radial power indices $q_\rho = 2.25$ for density and $q_T = 0.5$ for temperature (note that, at the mid-plane, this initial temperature profile is identical to the prescribed dust temperature profile in eq. 5). The disk mass is $\simeq 0.033 M_\odot$ within 50 au. Such hydrodynamic initial conditions generally follow B17; compared to WG17, this disk has $\sim 1.5\times$ the midplane scale height.

The initial abundances of the chemical species are set uniformly throughout the domain according to Table 1 (n_H is the number density of hydrogen nuclei). The abundances of elements generally follow a subset of those in Gorti & Hollenbach (2008, 2009) (note that the elemental abundances of S and Si are subject to depletion compared to the Solar abundances; see also Jenkins 2009), with the additional assumption that elements appear in chemical compounds if possible.

The initial poloidal fields are described by a purely azimuthal vector potential $\mathbf{A} \equiv A_\phi \hat{\phi}$, (Zanni et al. 2007),

$$A_\phi = \frac{B_0 r_0}{4 - \alpha - q_T} \left(\frac{R}{r_0} \right)^{1 - \frac{\alpha + q_T}{2}} [1 + (m \tan \theta)^{-2}]^{-5/2} , \quad (30)$$

where r_0 is some reference radius (we use $r_0 = 1 \text{ au}$), and B_0 is the midplane field intensity at r_0 , which is controlled by the plasma $\beta_0 \equiv 8\pi p_0/B_0^2$, p_0 being the

gas pressure at the midplane. Following B17, we choose $\beta_0 = 10^5$ for the fiducial model, which approximately yields disk accretion rate $\sim 10^{-8} M_\odot \text{ yr}^{-1}$,

$$B_p(\theta = \pi/2) = B_0 \left(\frac{R}{r_0} \right)^{-\frac{\alpha+q_T}{2}}. \quad (31)$$

In the vector potential (30), m is a control parameter that describes the bending of these initial poloidal fields; here we choose $m = 1$. As did B17, we have verified that reasonable variations of m do not affect the final quasi-steady state.

The boundary conditions deserve special attention in order to avoid unphysical results. As the innermost domain of $r < 1$ au is not included by our simulations, any fluxes (fluid, magnetic) emerging from the inner radial boundary should not affect the simulation domain. Since the standard outflow boundary conditions could violate causality and make the system unstable, we adopt boundary conditions similar to B17. Within the ghost zones for the inner boundary, the density and velocity are set according to the steady state solution used for the initial conditions, while the gas temperature and relative abundances of chemical species copy the values in the innermost radial zone. The magnetic fields are extrapolated from the innermost radial zone assuming $B_r \propto r^{-2}$, $B_\phi \propto r^{-1}$, and $B_\theta \propto r^0$. Inside the simulation domain we also set a radial buffer zone, $r \in [r_{\text{in}}, 1.5r_{\text{in}}]$, in which the MHD diffusivities are linearly tapered to zero as the radius decreases to r_{in} , and the poloidal velocity is damped at the local orbital timescale. This buffer zone helps to stabilize our simulations near the inner radial boundary. On the outer radial boundary, outflow boundary conditions (with inflow inhibitor) are applied to the fluid variables, while the scheme for magnetic fields is the same as at the inner radial boundary. The latitudinal boundaries are reflective: they keep the normal component of \mathbf{B} and flip tangential components.

3.4. Simulation Run

To relax hydrodynamic and thermochemical transients, we run the simulation for 2000 yr, from $t = -2000$ yr to $t = 0$, with hydrodynamics, radiation, and thermochemistry, but without MHD. Instantaneously, at $t = 0$, non-ideal MHD is turned on, and an external poloidal magnetic field described by eq. (30) is applied to the system. After that, this model is evolved to $t = 2000$ yr, by which time it has usually reached a quasi-steady state, except in unstable cases such as Model 7 (see below).

4. FIDUCIAL MODEL RESULTS

Table 1. Properties of the fiducial model

Item	Value
Radial domain	1 au $\leq r \leq$ 100 au
Latitudinal domain	$0.035 \leq \theta \leq \pi/2$
Resolution	$N_{\log r} = 384$, $N_\theta = 128$
Stellar mass	$1.0 M_\odot$
M_{disk} (1 au $\leq r \leq$ 100 au)	$0.033 M_\odot$
Initial mid-plane density	$2.38 \times 10^{14} (R/\text{au})^{-2.25} m_p \text{ cm}^{-3}$
Initial mid-plane plasma β	10^5
Initial mid-plane temperature	$280 (R/\text{au})^{-0.5} \text{ K}$
Artificial heating profile	$280 (R/\text{au})^{-0.5} \text{ K}$
Luminosities [photon s^{-1}]	
7 eV (“soft” FUV)	4.5×10^{42}
12 eV (LW)	1.6×10^{40}
25 eV (EUV)	0
3 keV (X-ray)	2.1×10^{38}
Initial abundances [n_X/n_H]	
H ₂	0.5
He	0.1
H ₂ O	1.8×10^{-4}
CO	1.4×10^{-4}
S	2.8×10^{-5}
SiO	1.7×10^{-6}
Gr	1.0×10^{-7}
Dust/PAH properties	
r_{dust}	5 Å
ρ_{dust}	2.25 g cm^{-3}
$m_{\text{dust}}/m_{\text{gas}}$	7×10^{-5}
σ_{dust}/H	$8 \times 10^{22} \text{ cm}^2$

Figure 1 exhibits meridional plots of the fiducial model (Model 0) averaged over the final 50 yr (from $t = 1950$ yr to 2000 yr) of the simulation, during which the model has already reached quasi-steady state: $\langle \dot{M}_{\text{wind}} \rangle_{50}$ (the 50 yr average of wind mass loss rate) exhibits less than $\sim 5\%$ r.m.s. variation during 10^3 yr. Black solid curves in the top and bottom row are streamlines, integral curves of the poloidal vector field $\rho \mathbf{v}_p$ spaced by constant wind mass loss rate $10^{-9} M_\odot \text{ yr}^{-1}$. White solid curves in the bottom row are magnetic field lines spaced by constant poloidal magnetic flux $5 \times 10^{25} \text{ G cm}^2$. Mass fluxes between neighboring stream lines are integrated over azimuth and are multiplied by two, to include both sides of the equatorial plane. The fluid streamlines are masked out below the wind base.

A stream or field line that originates from the disk at cylindrical radius $R_0 > 50$ au may not reach its poloidal Alfvénic point before it leaves the simulation domain at $r = 100$ au. Furthermore, the outer regions take

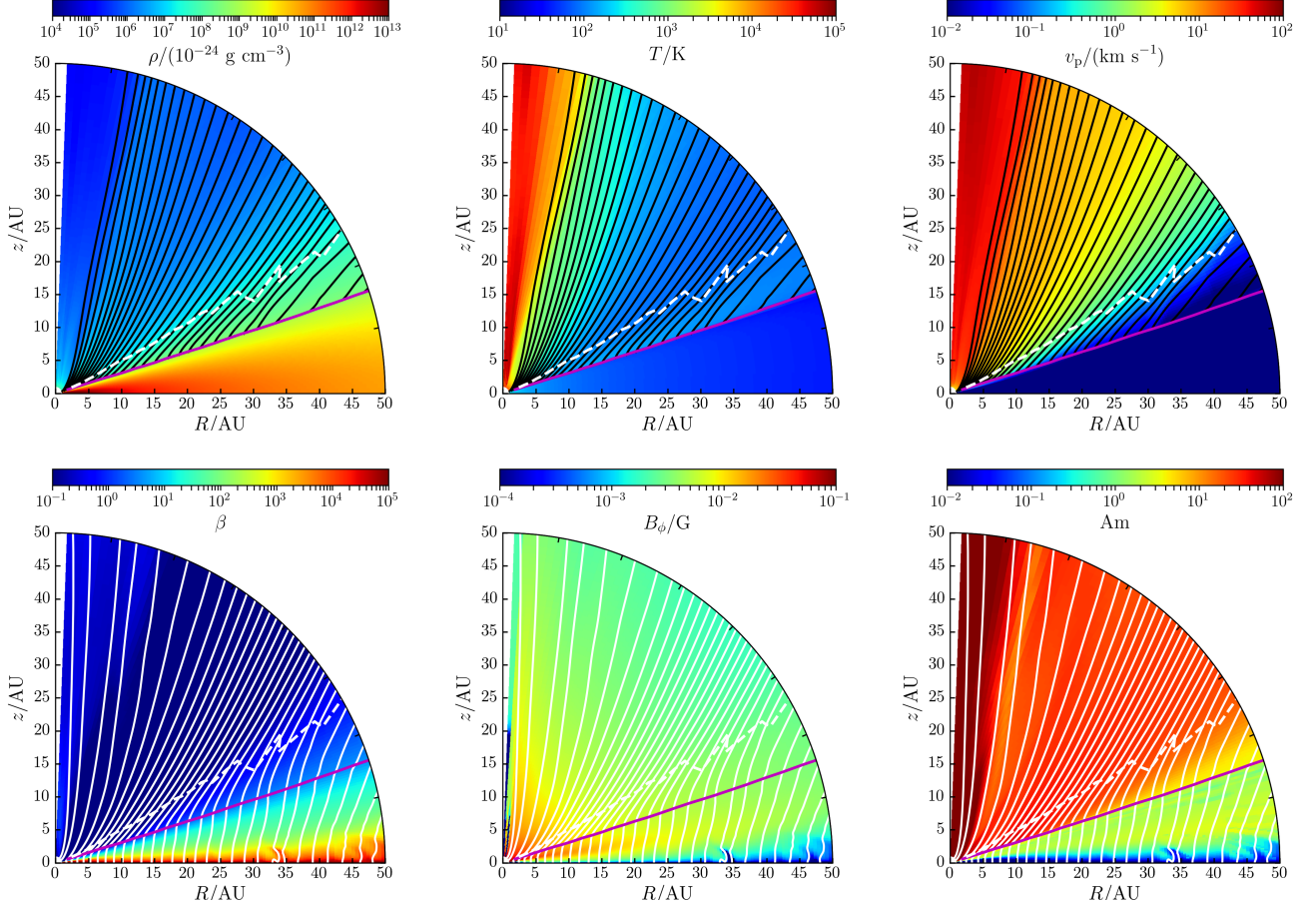


Figure 1. Meridional plots for the fiducial model (Model 0; §3), showing the innermost 50 au averaged over the final 50 yr. **Top row:** basic hydrodynamic profiles. *Left panel:* mass density in units of $10^{-24} \text{ g cm}^{-3}$; *middle panel:* temperature in Kelvin; *right panel:* poloidal velocity in units of km s^{-1} . **Bottom row:** MHD-related profiles. *Left panel:* plasma β ; *middle panel:* toroidal magnetic field in units of Gauss; *right panel:* ambipolar Elsasser number Am [eq. (12)]. *Black curves, upper panels:* poloidal streamlines separated by $10^{-9} M_{\odot} \text{ yr}^{-1}$. *White solid curves, lower panels:* poloidal magnetic field lines. *White dashed curves:* poloidal Alfvénic surface. *Magenta lines:* wind bases (defined as the FUV front, §2.4.2).

longer to reach steady state, often longer than 2000 yr. Therefore, in what follows, our analyses will be limited to $r < 50$ au.

In quasi-steady states, the outflow typically becomes super-Alfvénic within a factor or two or less in cylindrical radius beyond the wind base. Hence the outflow is a wind, rather than a sub-Alfvénic breeze; in what follows we will use the terms “wind”/“outflow” interchangeably unless specifically noted. If we integrate the radial outflow above wind bases over the sphere at $r = 50$ au, excluding streamlines emanating from the inner radial boundary, we obtain a total wind mass loss rate of $\dot{M}_{\text{wind}} \simeq 2.9 \times 10^{-8} M_{\odot} \text{ yr}^{-1}$. The mean radial outflow velocity weighted by radial mass flux is $\langle v_r \rangle \simeq 4.6 \text{ km s}^{-1}$. In the mid-plane, the radial accretion rate is almost constant with radius, varying slightly within the range $1.3\text{--}2.1 \times 10^{-8} M_{\odot} \text{ yr}^{-1}$. For the same 50 yr average, Figure 2 displays the run of several flow

variables along three representative magnetic field lines with footpoints on the equatorial plane at $R_0 = 2$ au, 10 au and 30 au. These plots will inform our analysis of the physics of the wind in the rest of this section.

4.1. Magnetohydrodynamics of Disk and Wind

4.1.1. Wind launching and kinematics

How is the disk wind launched? Before the poloidal magnetic field is applied, the fiducial simulation has been run for 2000 yr (§3.4), during which no appreciable outflow was observed ($\dot{M}_{\text{wind}} < 10^{-11} M_{\odot} \text{ yr}^{-1}$)—similar to the model without EUV in WG17. Evidently, magnetic fields are crucial for launching the wind, at least with our fiducial parameters (which omit EUV).

Figure 3 illustrates the force decomposition defined by eq. (14) along the field line originating from $R_0 = 10$ au, which we find representative for field lines at all radii. We note that the net inertial acceleration f_{ine} is negative

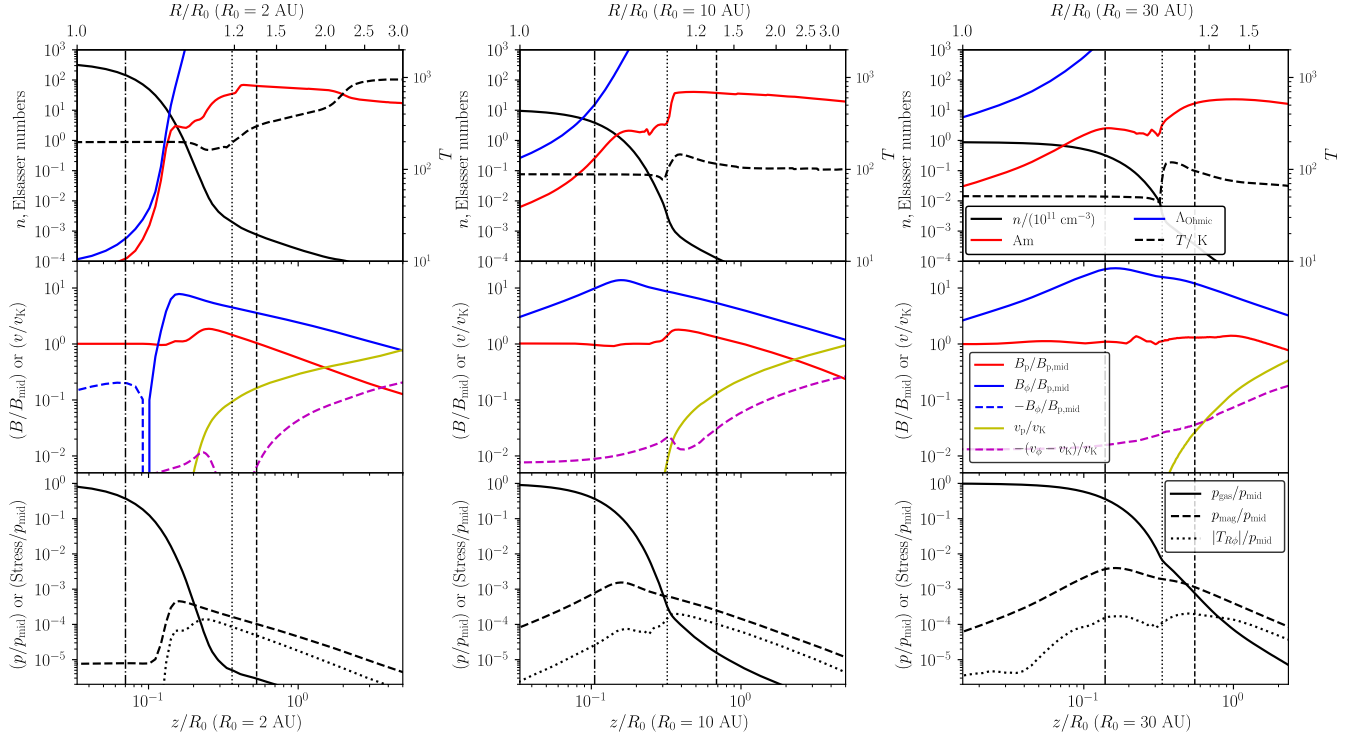


Figure 2. Flow profiles of the fiducial model (Model 0), averaged over the final 50 yr, along three different magnetic field lines, which intercept the equatorial plane at cylindrical radii $R_0 = 2$ au (left column), $R_0 = 10$ au (middle column), and $R_0 = 30$ au (right column). Normalized coordinates (R/R_0 , z/R_0) along field lines shown on upper & lower abscissae. Profiles are distinguished by line shape and color, as marked by the legends. Vertical dash-dotted, dotted and dashed lines in black indicate the midplane scale height (h_{mid}), the wind base (z_{wb} , the soft FUV front; §2.4.2), and the poloidal Alfvénic point, respectively.

First row: number density of hydrogen nuclei n , Ohmic & ambipolar Elsasser numbers Λ_{Ohmic} & Λ_{Am} [eq. (12)], and temperature T (right ordinate). Second row: poloidal (B_p) and toroidal (B_ϕ) components of the magnetic field (normalized to midplane value on the current field line, $B_{p,\text{mid}}$), and poloidal (v_p) and toroidal (v_ϕ) components of fluid velocity (normalized to the Keplerian velocity at the local cylindrical radius, $v_K \equiv \sqrt{GM_*/R}$). Third row: gas pressure (p_{gas}), magnetic pressure (p_{mag}) and (R, ϕ) component of Maxwell stress tensor ($T_{R\phi} \equiv -B_R B_\phi / 4\pi$), normalized by $p_{\text{mid}} \equiv p_{\text{gas}}|_{z=0}$.

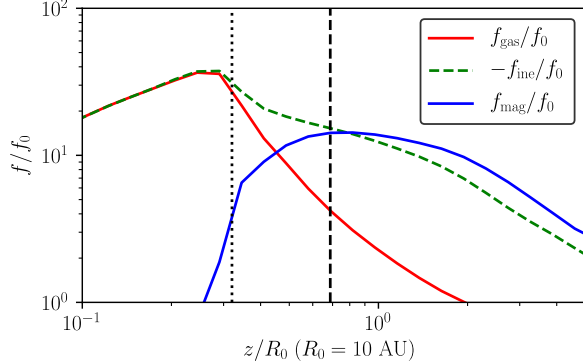


Figure 3. Poloidal forces [eq. (14)] along the field line anchored at $R_0 = 10$ au, averaged over the final 50 yr of Model 0. All forces are normalized to $f_0 \equiv p_{\text{mid}}/(R_0 \rho_{\text{mid}})$. Vertical dotted and dashed lines mark the wind base and poloidal Alfvénic point, respectively.

everywhere. In fact, the toroidal velocity v_ϕ is everywhere sub-Keplerian (see the second row of Figure 2). The magnetic field is too weak ($\beta_{\text{wind}} \gtrsim 10^{-1}$) to enforce

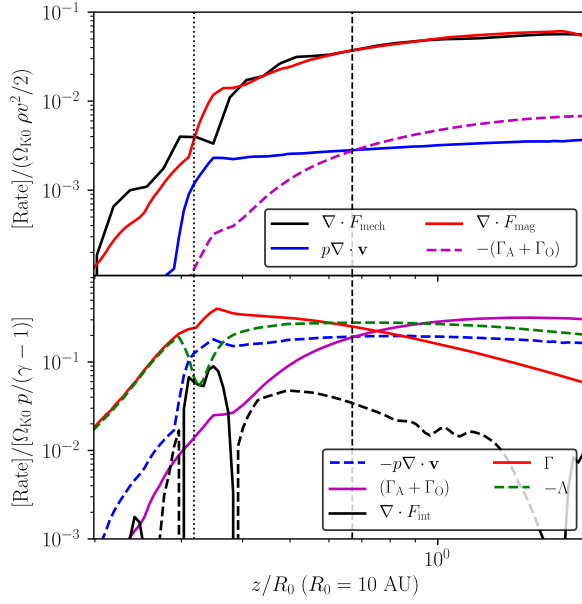
co-rotation, as would be required for magnetocentrifugal acceleration (see also Bai et al. 2016). Instead, the poloidal lines wind up into toroidal ones under the inertia of the fluid, and the combined thermal and magnetic pressures launch the wind. B17 has dubbed such winds “magneto-thermal.”

Above the wind base, toroidal fluid velocities start to deviate appreciably from the local v_K , and poloidal components become important, increasing to $v_p \sim 10^{-1} v_K$. Figure 5 displays the diagnostic quantities (16) along the $R_0 = 10$ au field line. These quantities are roughly but not strictly conserved, (e.g., field lines deviate from fluid streamlines, as is seen in Figure 1). We notice that the specific angular momentum l is approximately $1.7 \Omega_K(R_0) R_0^2$: a fluid element on this field line carries off only 70% more than its original Keplerian angular momentum as it flies to infinity, implying that the local wind mass loss rate should be comparable to the accretion rate.

Table 2. Model 0 wind energy budget.

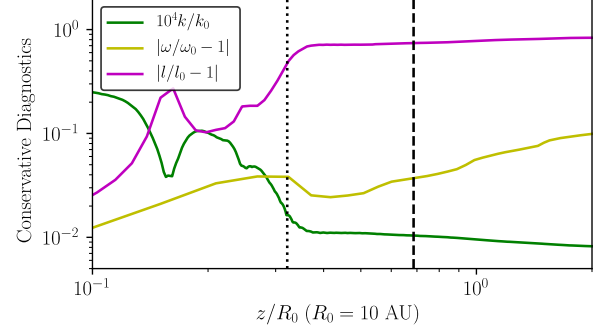
Item	Value [10^{30} erg s $^{-1}$]
\dot{E}_{mech}	1.40
$\dot{E}_{\text{k,p}}$	0.40
$\dot{E}_{\text{k},\phi}$	-1.06
\dot{E}_{grav}	2.05
\dot{E}_{pdV}	0.01
\dot{E}_{mag}	-1.53
\dot{E}_{stress}	-1.60
$\dot{E}_{\text{S'}}$	0.02
\dot{E}_{B}	0.05
\dot{E}_{int}	0.02
\dot{E}_{na}	0.10
\dot{E}_{heat}	-0.10
\dot{E}_{cool}	0.20

NOTE—See §2.4.4 and §4.1.2.

**Figure 4.** Local energy balance (eq. 20) along the field line anchored at $R_0 = 10$ au. *Upper panel:* $\nabla \cdot F_{\text{mech}}$ and associated quantities, normalized by $(\Omega_{\text{K}0} \rho v^2 / 2)$ ($\Omega_{\text{K}0}$ is the Keplerian angular velocity at R_0). *Lower panel:* $\nabla \cdot F_{\text{int}}$ and associated quantities, normalized by $[\Omega_{\text{K}0} p / (\gamma - 1)]$. Different components are distinguished by colors; line shape indicates the sign (solid: positive; dashed: negative). Vertical dotted and dashed lines in black indicate the wind base and the poloidal Alfvénic point, respectively.

4.1.2. Wind energy budget

Analysis on the energy budget combines Figure 4 and Table 2 for the fiducial model. We define the “wind region” as $\{z > z_{\text{wb}}\} \cap \{1.5 < (r/\text{au}) < 50\}$; the $1 <$

**Figure 5.** Like Figure 3 but for the wind “constants” (k, ω, l) defined in eq. (16).

$(r/\text{au}) < 1.5$ zone is excluded due to numerical damping near the inner boundary (§3.3).

The upper panel of Figure 4 clearly indicates that the mechanical power of the wind comes predominantly from the magnetic field. This is confirmed by Table 2 with a significant negative \dot{E}_{stress} , indicating that the wind is driven by the work that magnetic stress does on the wind base, ultimately at the expense of the orbital energy of the disk. Another important source of power is the toroidal motion of the gas ($\dot{E}_{\text{k},\phi} < 0$), which is converted to the other forms of mechanical power inside the wind. The majority of power injected is expended in overcoming the negative gravitational energy of the gas; the poloidal kinetic energy consumes the second most of the injected power.

We notice that hard-photon heating is rather inefficient. Out of the total hard-photon luminosity radiated by the central star $L_{\text{tot}} \simeq 5.2 \times 10^{31}$ erg s $^{-1}$, only $L_{\text{abs}} \simeq 6.2 \times 10^{30}$ erg s $^{-1}$ is actually absorbed. Eventually, less than 2 % of L_{abs} is converted to heat: most of rest is consumed by photodissociation, photoionization and photoelectric processes, and for maintaining T_{dust} (see also appendices of WG17). However, radiative heating does play an important role in affecting the internal energy density near the wind base, as we can observe in the lower panel of Figure 4. At higher altitudes (roughly above the poloidal Alfvénic point), heating due to non-ideal MHD dissipation, especially by ambipolar diffusion. In total, ambipolar diffusion converts magnetic and kinetic energy into heat at 0.56×10^{30} erg s $^{-1} > |\dot{E}_{\text{heat}}|$. Further discussions of ambipolar heating is postponed to §5.3.

4.1.3. Magnetic field profiles

The poloidal field lines of the fiducial model are almost vertical near the midplane due to large diffusivities there. Although the mid-plane diffusivity is not captured very accurately, this behavior is largely consistent with B17. Above the midplane in the wind, stronger

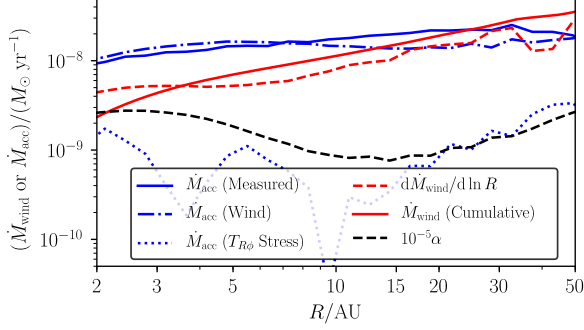


Figure 6. Radial profiles of mass dispersal rates in the fiducial model (Model 0). Accretion rates contributed by wind and $T_{R\phi}$ Maxwell stress are estimated by eq. (18). The Shakura-Sunyaev α parameter for radial angular momentum transport (eq.19) is also presented.

field-fluid coupling bends the poloidal field lines radially outwards. The toroidal component B_ϕ dominates at almost all radii and altitudes. This component should change sign across the equatorial plane due to our reflecting boundary conditions at the equatorial plane.

4.1.4. Angular momentum budget and accretion

In Figure 6 compares the accretion rates driven by different angular momentum transport mechanisms (eq. 18). Clearly, vertical transport of angular momentum radial transport by a significant factor. We find that the local wind mass loss rate is always comparable to the accretion rate, as already discussed in §4.1.1. The radial Maxwell stress can be characterized by the equivalent α (eq. 19). Over the entire radial range of the fiducial simulation, $\alpha \lesssim 3 \times 10^{-4}$.

At small radii ($R \lesssim 20$ au), we find $R_A/R_{wb} \simeq 1.4$ and $\xi \simeq 0.5$. The lever arm decreases to $R_A/R_{wb} \sim 1.15 \pm 0.02$ at larger radii, corresponding to bigger $\xi \simeq 1$. These trends can be seen in Figure 6. Thus while the magnetized wind produces a reasonable accretion rate—by construction—it does so rather inefficiently, with an even larger outflow rate. We expect that a larger ejection index and a more nearly magnetocentrifugal (rather than magnetothermal) wind could be obtained by increasing the magnetization (β_0^{-1}). But Model 7 (§5) suggests that to maintain accretion rates comparable to what is observed, the surface density of the disk would then have to be reduced (e.g., Wang & Goodman 2017b).

Figure 7 exhibits vertical profiles of the radial mass flux at two representative cylindrical radii, $R = 2$ au and 10 au. The accreting layer is centered at the midplane at $R = 10$ au, but at $|z| \simeq 1.5h_{\text{mid}}$ at $R = 2$ au, evidently because the midplane is too weakly ionized and poorly coupled in the latter case. The dashed curves in the figure indicate radial mass-flux profiles predicted by taking the vertical gradient of $T_{z\phi}$ stress. These predictions are

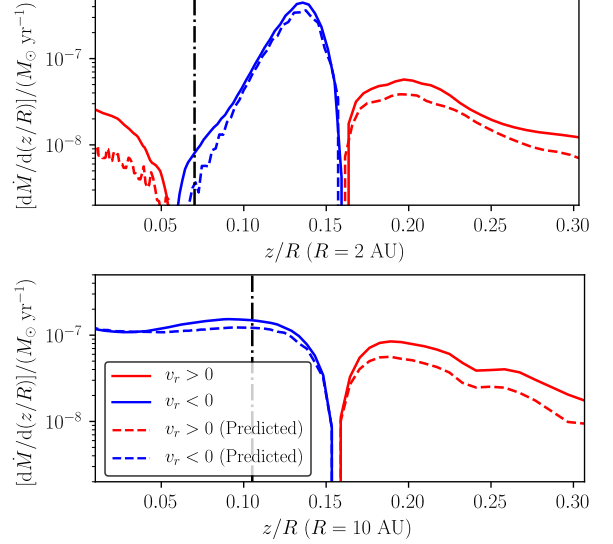


Figure 7. Vertical profiles of local mass flux [in $M_\odot \text{ yr}^{-1}$ per (z/R)] at $R = 2$ au and $R = 10$ au for Model 0 plotted below the wind base. Blue and red colors indicate accretion and decretion/outflow, respectively. Solid lines are measured directly from the simulation, while dashed curves are values predicted by taking vertical gradients of $T_{z\phi}$ magnetic stress. Vertical dash-dotted line in black indicates h_{mid} , the gaussian scale height at the midplane.

consistent with with direct measurements of the flux, verifying that vertical transport of angular momentum (and hence wind launching) mediated by the $T_{z\phi}$ stress is indeed the predominant mechanism that drives disk accretion. There is a layer of radial outflow above the accretion layer and below the wind base. This outflow, like the accretion inflow, is driven by the $B_\phi B_z$ magnetic stress, but with the opposite sign of the vertical gradient as dB_ϕ/dz changes its sign. Such outflow is always subsonic and sub-Alfvénic; nor does the flow actually join the wind. In order to distinguish it from the wind, we describe this “dcretion layer” in what follows. The total outward mass flux in the decretion layer is $\lesssim 15\%$ of the accretion. This decretion layer is a generic feature that is also present below the wind base in the Hall-free simulations of B17. However, as discussed in B17, the flow structure in wind-driven accretion disks depends on the gradient of B_ϕ , which is sensitive to the diffusivity profiles within the disk. In this work, our diffusivity profile is not necessarily realistic near the midplane (§2.3), thus we generally view the flow structures there with caution.

4.2. Thermochemistry and Radiation

The interaction between magnetic fields and fluids is determined by radiation and thermochemical processes. In this subsection, we analyze the microphysics for

three different layers: the midplane (§4.2.1), the wind-launching region (§4.1.1), and the upper wind (§4.2.3).

4.2.1. Midplane region

The dust and gas temperatures near the midplane are maintained somewhat artificially by the prescriptions described in and around eqs. (4)-(5). Nevertheless, as this region is largely shielded from hard photons and poorly coupled to the magnetic field, it would not be appreciably affected by photoionization/photodissociation heating or non-ideal MHD heating in any case. Its thermal state should properly be regulated by the diffuse infrared radiation field, and by thermal accommodation between dust and gas.

Though unimportant for the temperature near the midplane, the hard photons are important for the ionization there. Grains are the dominant charge carriers. At small radii ($R \lesssim 2$ au), the ionization is very weak the vertical column above is too massive for diffuse sources of ionization (scattered X-ray photons and cosmic rays) to penetrate. The Elsasser numbers are therefore tiny, $Am \ll \Lambda_{\text{Ohmic}} \lesssim 10^{-4}$ at $R = 2$ au. Eased penetration at relatively larger radii raises the level of ionization, and the Elsasser numbers rise accordingly: on the midplane at 10 au, $\Lambda_{\text{Ohmic}} \sim 10^0$ and $Am \gtrsim 10^{-2}$. The radial variation of midplane ionization also leads to the change of magnetic field morphology, as we discussed in §4.1.3.

4.2.2. Wind-launching region

At higher altitudes, the transition from a poloidally static midplane layer to an appreciable outflow takes place near the wind base at $3h_{\text{mid}} \lesssim z \lesssim 4h_{\text{mid}}$.

The gas density is lower by a factor $\sim 10^{-4}$ to 10^{-5} than at the midplane. Penetration is eased for cosmic rays and scattered X-rays, and especially for high energy photons propagating directly from the protostar. Thanks to these processes, the gas temperature rises to about twice that of the local midplane. The hard photons also yield a considerably higher level of ionization. As the absolute abundance of charge increases to $\sim 10^{0\pm1} \text{ cm}^{-3}$ (fractional ionization $\sim 10^{-7\pm1}$), the ambipolar Elsasser number Am becomes $\sim O(1)$. The dominant charge carriers are S^+ and Si^+ , while carbon is almost neutral since photoionization of CO and C are more susceptible to cross-/self-shielding effects, especially by H_2 .

4.2.3. Wind region

The physics is relatively straightforward inside the outflow. The gas continues to be accelerated by the magnetic pressure gradient all the way through the Alfvénic point. The low gas density and column density allows

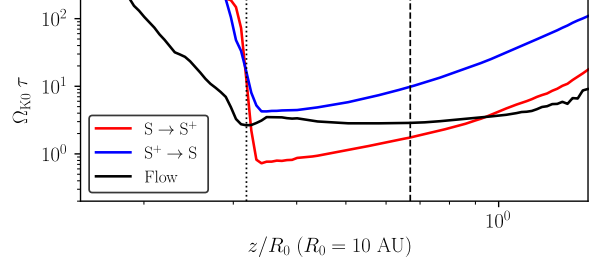


Figure 8. Timescales of hydrodynamic flow, and radiative ionization and recombination of sulfur along the field line anchored at $R_0 = 10$ au (eq. 32). All timescales are normalized by Ω_{K0} , the Keplerian angular velocity at $R_0 = 10$ au.

more ionizing photon to get in, hence the ambipolar Elsasser number reaches $30 \lesssim Am \lesssim 10^2$. Even such an Am allows some drift between charged and neutral particles, therefore field lines and streamlines do not perfectly coincide, and there is significant ambipolar heating.

The temperature of the wind is determined by the balance between ambipolar diffusion heating (the leading heating mechanism), and adiabatic expansion (for the outflow launched from $R \lesssim 5$ au) and/or atomic/molecular cooling (for the outflow launched by the $R \gtrsim 5$ au). Radiative heating is relatively ineffective because of the small X-ray cross section, strong cross-shielding of LW photons, and depletion of molecular species susceptible to dissociation by soft FUV. At relatively large radii, the gas temperature drops slightly as fluids move outwards, since the sum of adiabatic and radiative cooling mechanisms exceeds non-ideal MHD heating (see Figures 2, 4).

Figure 9 plots the distributions of several key chemical species in velocity and temperature. We notice a prominent tail of neutral atomic/molecular species inside the wind, located at relatively high temperature ($T \gtrsim 10^3$ K) and intermediate poloidal velocity ($v_p \sim 15 \text{ km s}^{-1}$). In Table 3, we present the mass-loss rates of key species. The magneto-thermal wind is predominantly molecular, thanks to its high density in comparison to the unmagnetized EUV-driven winds studied by WG17. Note that abundances of those species cannot be correctly calculated if we assume local thermochemical equilibrium instead of evolving thermochemical networks in real-time. As an example, we compare the flow timescale to the timescales of radiative ionization and recombination of sulfur along a field line. We define these as,

$$\begin{aligned} \tau_{\text{flow}} &\equiv \left| v_p \frac{d \ln \rho}{ds} \right|^{-1}, \quad \tau_{S \rightarrow S^+} \equiv \frac{n(S)}{k(h\nu + S \rightarrow e^- + S^+)}, \\ \tau_{S^+ \rightarrow S} &\equiv \frac{n(S^+)}{k(S^+ + e^- \rightarrow S)}, \end{aligned} \quad (32)$$

Table 3. Mass-loss rates of several species in Model 0.

Species	\dot{M}	$\dot{M}/\dot{M}_{\text{wind}}$
	($M_{\odot} \text{ yr}^{-1}$)	
H ₂	1.91×10^{-8}	6.97×10^{-1}
H	5.64×10^{-10}	2.06×10^{-2}
H ⁺	2.56×10^{-14}	9.34×10^{-7}
He	7.81×10^{-9}	2.85×10^{-1}
He ⁺	1.90×10^{-14}	6.93×10^{-7}
H ₂ O	9.01×10^{-13}	3.29×10^{-5}
OH	2.21×10^{-12}	8.07×10^{-5}
CO	5.38×10^{-11}	1.96×10^{-3}
O	6.67×10^{-11}	2.43×10^{-3}
O ⁺	7.80×10^{-17}	2.84×10^{-9}
C	9.02×10^{-12}	3.29×10^{-4}
C ⁺	7.00×10^{-13}	2.55×10^{-5}
S	1.07×10^{-11}	3.89×10^{-4}
S ⁺	6.84×10^{-12}	2.49×10^{-4}

where the derivative in τ_{flow} is taken with respect to arc length s along the field line, and k denote the reaction rates. In Figure 8, at all altitudes above the wind base, τ_{flow} is comparable to the timescales of ionization and recombination.

We attribute the co-existence of CO and C⁺ in the wind to shielding effects: in the LW band, CO photodissociation is more sensitive to self-shielding and especially to cross-shielding by H₂, compared to photoionization of CO and C. As a result, although LW photons penetrate deeply near the wind base, CO still exists there.

H₂O and OH molecules are mainly dissociated by the soft FUV continuum, hence they are not sensitive to shielding effects and do not survive in significant numbers in the wind. Instead, oxygen exists mostly in atomic form, with poloidal velocity ($v_p \sim 15 \text{ km s}^{-1}$). At high latitudes, however, where $T \sim 10^3 \text{ K}$ and $n(\text{H}_2) \sim 10^{6-7} \text{ cm}^{-3}$, result in the re-formation rates of H₂O and OH are competitive with photodissociation (see the upper-left and upper-middle panels in Figure 1, and the upper left panel in Figure 9). For example, at $r = 5 \text{ au}$ and $0.2 \lesssim \theta \lesssim 0.4$ in our fiducial model, the major destruction mechanism of OH molecules is photodissociation by soft FUV photons, the rate per OH molecule being $\xi \simeq 3 \times 10^{-5} \text{ s}^{-1}$ (absorption ignored). At $T \simeq 10^3 \text{ K}$ and $n(\text{H}_2) \simeq 10^7 \text{ cm}^{-3}$, the rate at which an oxygen atom re-forms OH is approximately (according to the UMIST database; see McElroy et al. 2013) $3 \times 10^{-6} \text{ s}^{-1}$, via the most important reaction channel $\text{O} + \text{H}_2 \rightarrow \text{OH} + \text{H}$. As a result, $\sim 10 \%$ of the oxygen resides in OH molecules. These re-formed H₂O/OH molecules mainly appear at very high latitudes and intermediate radial velocity ($v_r \sim 10 - 40 \text{ km s}^{-1}$),

Table 4. Various models for parameter study

Model	$\dot{M}_{\text{acc}}(10 \text{ au})$	\dot{M}_{wind}	$\langle v_r \rangle$
	($10^{-8} M_{\odot}/\text{yr}$)	($10^{-8} M_{\odot}/\text{yr}$)	(km s^{-1})
(1)	(2)	(3)	(4)
0 (Fiducial)	1.7 ± 0.3	2.9 ± 0.2	4.6 ± 0.4
0 ⁻ (Convergence test)	1.9 ± 0.5	2.7 ± 0.4	4.0 ± 0.3
0 ^γ ($\gamma = 1.4$)	1.3 ± 0.3	2.7 ± 0.2	4.4 ± 0.6
1 (Ambipolar heating off)	1.7 ± 0.3	2.8 ± 0.3	4.7 ± 0.3
2 ($0.1 \times \text{X-ray}$)	1.2 ± 0.4	2.7 ± 0.3	6.0 ± 0.3
3 ($0.1 \times \text{Soft FUV}$)	1.7 ± 0.4	2.4 ± 0.3	5.5 ± 0.7
4 ($0.1 \times \text{LW}$)	1.6 ± 0.3	2.6 ± 0.2	5.0 ± 0.5
5 ($0.1 \times \text{All hard photons}$)	1.1 ± 0.5	1.4 ± 0.4	7.5 ± 1.2
6 ($\Phi_{\text{EUV}} = 10^{41.7} \text{ s}^{-1}$)	1.5 ± 0.4	1.6 ± 0.1	8.5 ± 0.6
7 ($\beta_0 = 10^4$)	17.1 ± 1.5	16.6 ± 3.3	6.7 ± 0.7
8 ($0.1 \times \text{Dust grains}^*$)	7.4 ± 0.8	5.1 ± 1.5	3.4 ± 4.5

NOTE— (1) Model identifier and description (parameter by which model differs from fiducial). (2) Accretion rate measured at $R = 10 \text{ au}$. (3) Wind mass-loss rate. (4) Mean outflow velocity (weighted by mass flux). Measurements are averaged over the final 50 yr of each simulation. Quoted errors are twice the r.m.s. time variation.

*: This model exhibits instabilities; see §5.6

and of course at $T \sim 10^3 \text{ K}$. The distribution of these molecules could be checked observationally and used to constrain wind models.

5. PARAMETER STUDY

To explore the sensitivity of our results to our input parameters, we performed a number of additional simulations, each differing from the fiducial run in one parameter. These simulations are described in §5.1 and summarized in Table 4.

5.1. Parameter variations

Model 0⁻ tests the convergence of our simulations, repeating the fiducial run on a 192×64 grid, i.e. 2 times coarser in both latitudinal and radial zones. Model 0^γ recalculates the fiducial model with $\gamma = 1.4$ rather than $\gamma = 5/3$ in the hydrodynamic solver.

Our analyses in §4.2 show that heating by non-ideal MHD effects could be important in at least some regions of the wind-launching system. Model 1 further explores this by turning off such heating processes.

According to WG17, the the spectral-energy distribution of the high-energy radiation is crucial for shaping photoevaporative outflows in the absence of magnetic fields. One major concern is therefore how different bands of radiation affect MHD outflows. Specifically, the fiducial model omits EUV radiation for better comparison with B17. This may not be realistic, as EUV may still reach the top of the wind—i.e., the parts nearest the axis, which have the lowest radial column den-

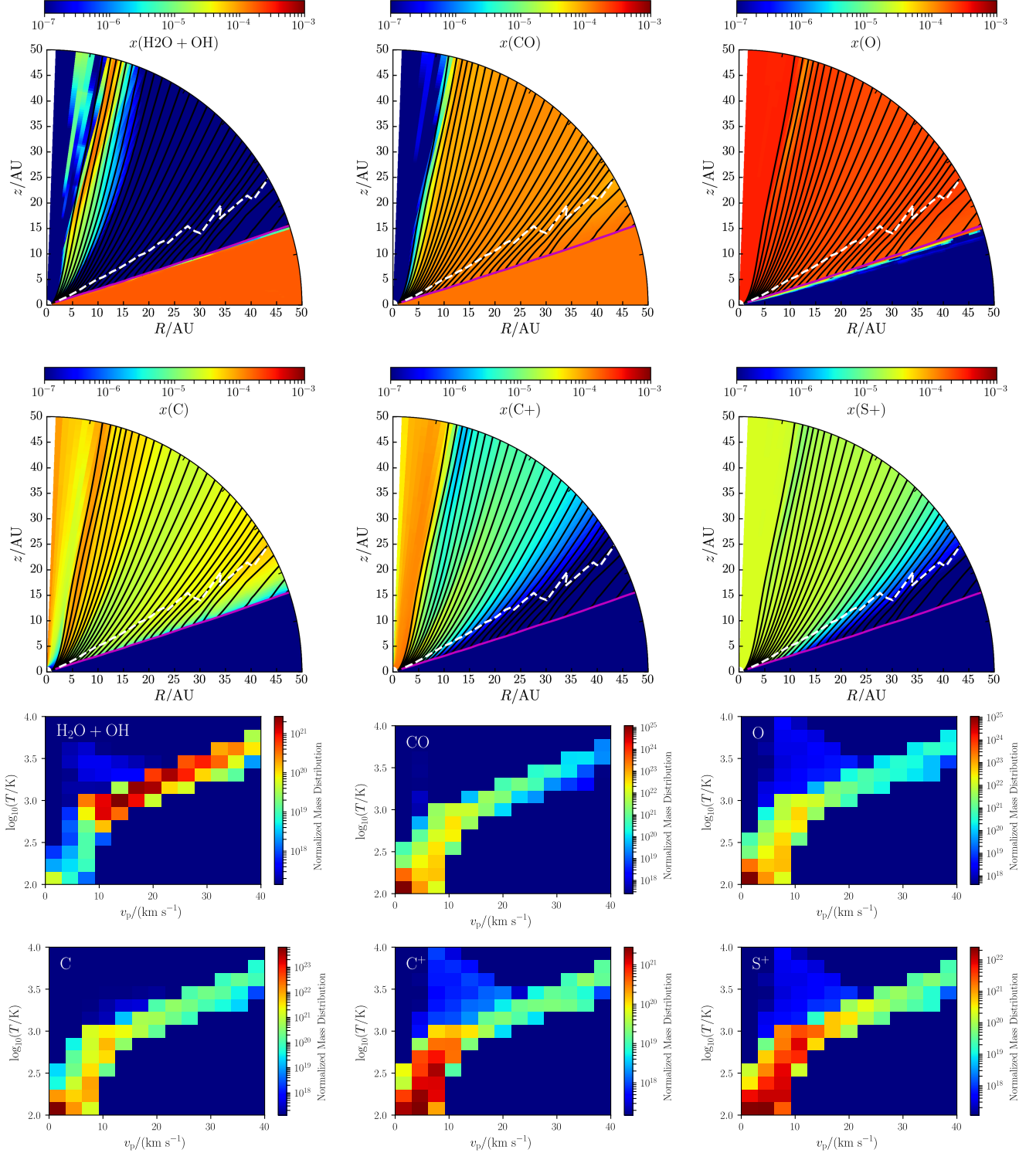


Figure 9. Distribution of key species in Model 0: H₂O/OH, CO, O (atomic oxygen), C (atomic carbon), C⁺, and S⁺. Top two rows show their spatial distribution, while bottom two rows present their distributions in the two-dimensional space of poloidal speed v_p and logarithm of temperature. The normalized mass distribution represents $d^2m/[d\log_{10}(T/K)d(v_p/\text{km s}^{-1})]$. Streamlines, wind bases, and Alfvénic surfaces are indicated in the top two rows as in Figure 1.

sity. Models 2 through 6 examine the importance of radiation, especially EUV, by varying the luminosities in each energy band.

The magnetic field plays a central role in transporting angular momentum and hence disk dispersal. Model 7 examines the impact of increased magnetization by setting midplane plasma $\beta_0 = 10^4$.

Models 8 varies the abundance of dust grains. Arguments in Geers et al. (2006); Tielens (2008); Woitke et al. (2016) suggest that our PAH abundance is roughly 4 to 10 times the ISM standard. This is deliberate, because we use PAH as a proxy for all dust grains. Model 8, however, reduces the abundance of PAH by a factor of 10.

5.2. Numerical effects

The grid resolution and the restriction to a constant adiabatic index in the hydrodynamic solver are numerical or algorithmic limitations rather than astronomical or physical uncertainties. Model 0⁻ shows almost identical MHD profiles and consistent wind mass loss rates to those of the fiducial model, thus verifying the convergence of the latter.

According to Bai et al. (2016), wind mass loss rates should be relatively insensitive to the adiabatic index. Model 0⁺ appears to confirm this, although the accretion rate decreases by $\sim 20\%$. Fully detailed and consistent treatment will require nontrivial technical improvements to the hydrodynamic solver that are left to future works.

5.3. Heating, ionization, diffusivity and dynamics

We have suggested that microphysics is important for the launching and structure of PPD winds. Nevertheless, Models 1 through 5 are qualitatively similar to the fiducial model, though with some quantitative differences in outflow or accretion rate.

Despite the neglect of ambipolar heating in Model 1, the quantitative results are indistinguishable from the fiducial within their errorbars. This is apparently because, as Figure 4 shows, non-ideal MHD heating is important—in the sense that the associated heating timescale is comparable to the flow timescale—only at relatively high altitudes, where the wind is already super-Alfvénic. Nevertheless, the neglect of non-ideal MHD heating lowers the wind temperature to $T \sim 300$ K, compared to $T \sim 10^3$ K in the fiducial model at $0.3 \lesssim \theta \lesssim 0.6$. Safier (1993); Garcia et al. (2001) suggested that ambipolar heating might be important in PPD wind structures. Our results suggest that, at least in these magneto-thermal winds, such heating is more important for the temperature of the wind than for its outflow speed or mass-loss rate.

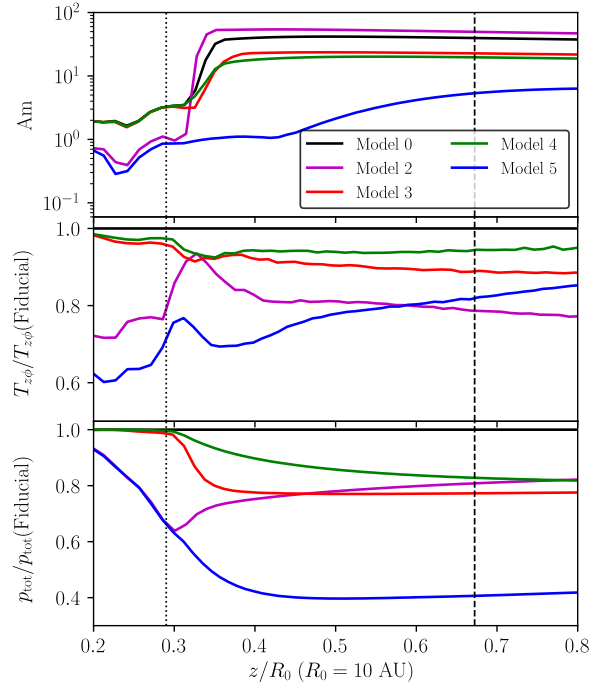


Figure 10. Ambipolar Elsasser number (top panel), $z - \phi$ Maxwell stress $T_{z\phi}$ (middle panel) and total pressure p_{tot} (bottom panel) for Models 0, 2, 3, 4, 5, along field lines anchored at $R_0 = 10$ au. $T_{z\phi}$ and p_{tot} profiles are normalized to those of the fiducial model (Model 0). Vertical dotted and dashed lines mark the wind base and the poloidal Alfvénic point of Model 0, respectively.

Models 2 through 5 test the response to reductions in the various hard-photon luminosities. Reduction of the X-ray luminosity has the greatest effect on the accretion rate (Model 2), while reduction of the soft-FUV and LW luminosities affect the wind mass-loss rate more than the accretion rate.

What is the underlying reason for the decreased accretion and mass-loss rates? In principle, \dot{M}_{wind} can be reduced by reducing the heating rate at the wind base. However, as we can observe from Table 2, radiative heating takes a small share ($\sim 5\%$) in the total energy balance of the wind; it can only affect wind launching weakly. Instead, both wind and accretion are driven mainly by magnetic fields, whose effect can be undercut by reducing the coupling between the gas and the field (reducing Am).

For lower X-ray luminosity, this undercutting happens most in and near the midplane. Scattered X-rays are the dominant ionization mechanism immediately below the wind base, as their absorption length is the longest among the hard-photon bands. With an X-ray luminosity ten times less than that of the other models, Model 2 has an Am near and below the wind base that is reduced by $\sim 2 - 3$ times. The weaker coupling leads

to weaker toroidal fields by $\sim 20\%$; this reduces both the toroidal magnetic pressure that helps to propel the outflow ($\propto B_\phi^2$), and also the torque on the disk that drives accretion ($\propto T_{z\phi} \propto B_\phi B_z$), as we can observe in Figure 10.

Soft-FUV and LW photons do not efficiently penetrate below the wind base; their luminosities do not affect the gas-field coupling there. Thus Models 3 and 4, with the same X-ray luminosity as the fiducial model, do not have appreciable difference in the wind-base $T_{z\phi}$ stress profiles and the accretion rates. Instead, their reduced luminosities in soft-FUV or LW result in weaker coupling only above the wind bases, reducing toroidal magnetic pressure and hence the wind mass-loss rates.

Model 5 is fainter than the fiducial model in all hard photon bands (excepting EUV, which both models lack entirely). It has similar rate of accretion as Model 2 due to lower X-ray luminosity, while the reduction in wind mass-loss rate combines the influence.

5.4. EUV Hybrid Wind

EUV photons have much larger absorption cross sections on hydrogen and helium than FUV and X-ray photons, and hence can only penetrate a radial column $N_H \sim 10^{18} \text{ cm}^{-2} \sim 10^5 \text{ cm}^{-3} \times 10 \text{ au}$. Thus, compared to these other high-energy bands, the EUV heats a smaller amount of mass to much higher temperatures. With the addition of EUV, Model 6 adds a fast component to the outflow that is not present in the fiducial model.

We present meridional plots of Model 5 in Figure 11. The most prominent feature is that the outflow is a hybrid of two components. Above a magneto-thermal wind that is qualitatively similar to that of non-EUV models, there is a fast EUV wind, in which the gas temperature rises to $T \sim 2 \times 10^4 \text{ K}$ and poloidal velocities reach $v_p \sim 40 - 80 \text{ km s}^{-1}$. This fast wind “steals” $\sim 0.26 \times 10^{-8} M_\odot \text{ yr}^{-1}$ from the magneto-thermal wind beneath.

Figure 12 illustrates the force decomposition along the field line emanating from $R_0 = 5 \text{ au}$, in which we can easily recognize the EUV front at $z/R_0 \simeq 3$. The contributions of the magnetic pressure gradient f_{gas} and of the gas pressure gradient f_{mag} are comparable in launching this wind. Obviously f_{gas} is dominated by EUV heating above the wind base. The rapid acceleration and expansion of the flow just above the base causes an abrupt decrease in magnetic field strength (see also lower-middle panel of Figure 11) and thus a significant gradient of magnetic pressure, which is reflected by a peak in f_{mag} .

In the magneto-thermal wind, Model 6 has a lower mass-loss rate than Model 0. In Figure 13 we com-

Table 5. Model 6 wind energy budget.

Item	Magneto-thermal wind	EUV wind
	[$10^{30} \text{ erg s}^{-1}$]	[$10^{30} \text{ erg s}^{-1}$]
\dot{E}_{mech}	0.75	1.97
$\dot{E}_{k,p}$	0.06	1.72
$\dot{E}_{k,\phi}$	-0.74	-0.22
\dot{E}_{grav}	1.40	0.41
\dot{E}_{pdV}	0.01	0.06
\dot{E}_{mag}	-0.90	-0.67
\dot{E}_{stress}	-1.14	-0.28
$\dot{E}_{S'}$	0.27	-0.33
\dot{E}_{B}	-0.03	-0.06
\dot{E}_{int}	0.02	0.09
\dot{E}_{na}	0.13	-1.38
\dot{E}_{heat}	-0.11	-2.02
\dot{E}_{cool}	0.24	0.63

pare these two models by showing vertical profiles at $R = 5 \text{ au}$. Launching of the EUV wind exerts pressure on the gas below the EUV front. The magneto-thermal wind adjusts itself to the extra pressure by converging to a new state that has higher temperature and similar density profile compared to its counterpart in the fiducial model. This higher temperature is maintained by increased ambipolar dissipation, which in turn is a result of reduced ion density due to faster recombination at higher temperature. For example, the re-formation rates of OH and H_2O molecules (H_xO) are faster in the magneto-thermal wind of Model 6, which subsequently yields more molecular ions (e.g. HCO^+) by charge exchange reactions. Because these molecular ions are very efficient eliminator of free electric charges via dissociative recombination, coupling between the gas and the field is weaker in the magneto-thermal wind layer, leading to the contrast the ambipolar Elsasser number profiles presented in Figures 1 versus 11. This effect further reduces the magnetic pressure in Model 6, and ultimately the wind mass loss rate.

The energy budget of Model 6 is presented by Table 5 and Figure 15, where the global wind budgets are calculated for the magneto-thermal and EUV winds separately (we use the EUV front to distinguish the hot EUV wind from the warm magneto-thermal wind). The magneto-thermal wind region is similar to but less energetic than Model 0. The EUV wind region, on the other hand, shows qualitative differences. Radiative heating overwhelms magnetic stress and toroidal kinetic power in adding energy to the wind. As the EUV wind is rather fast and launched from relatively high altitudes, the ma-

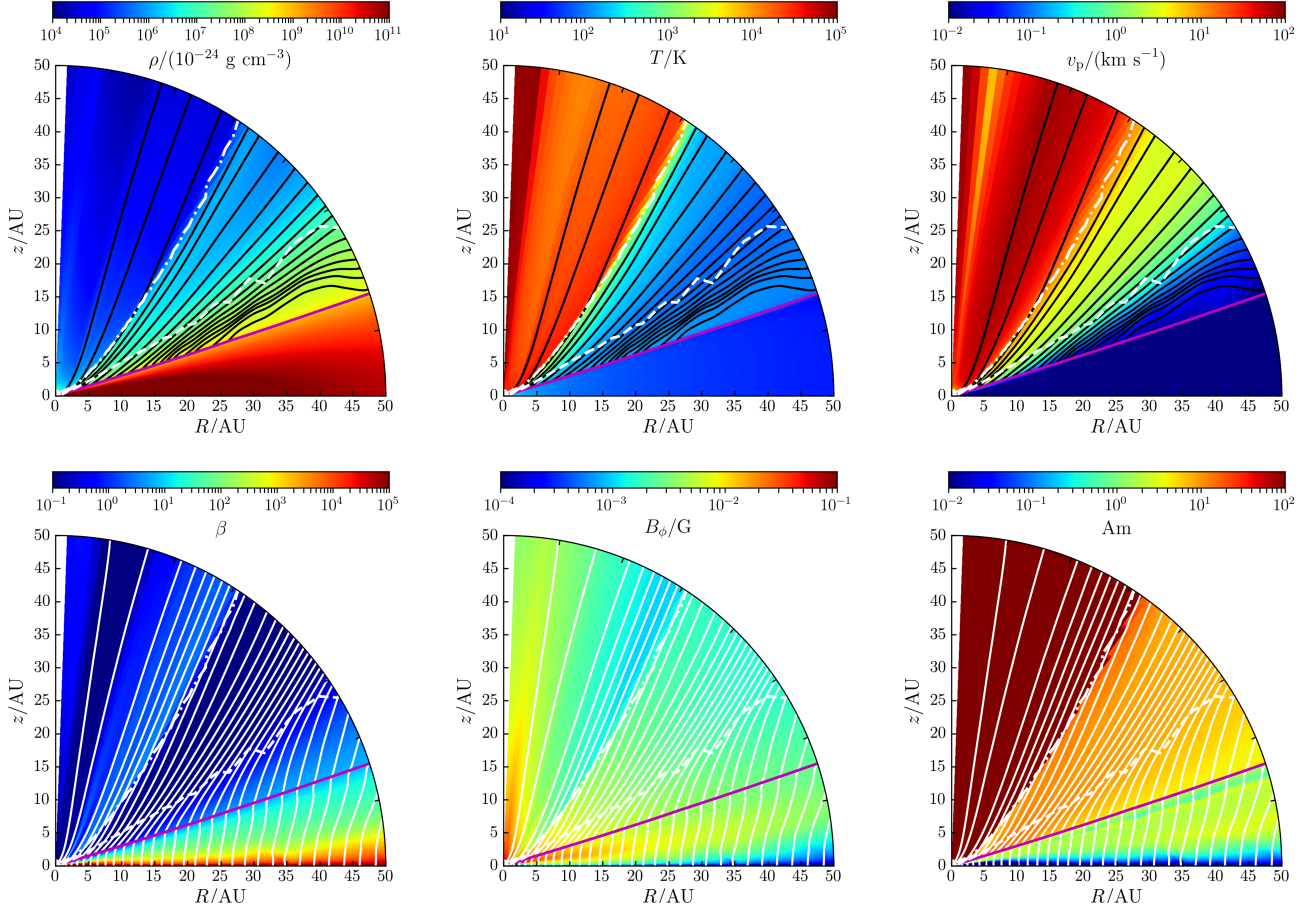


Figure 11. Same as Figure 1, but plotted for Model 6. White dash-dotted curves indicate the EUV front.

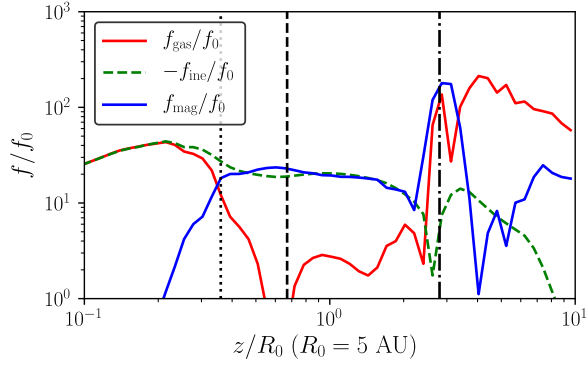


Figure 12. Like Figure 3, but for a field line anchored at $R_0 = 5$ au in Model 5. Vertical dash-dotted line indicates the EUV front.

jority of its mechanical power resides in the poloidal motion, instead of doing work against stellar gravity.

Table 6, compared to its counterpart for Model 0 (Table 3), clearly illustrates that the EUV-dominated layer contributes a predominantly ionized flux to the total outflow. Inspecting Figure 14, one sees that the distribution functions in the $\{\log_{10} T\} \times \{v_p\}$ plane of CO

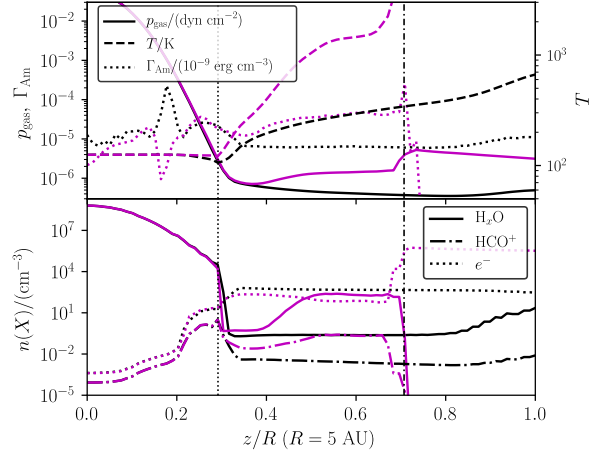


Figure 13. Comparison of vertical profiles at $R = 5$ au for Models 0 and 6. *Upper panel:* gas pressure p_{gas} (left ordinate), ambipolar heating rate Γ_{Am} (left ordinate), and temperature T (right ordinate). *Lower panel:* abundances of H_xO (H_2O and OH combined; lower panel), HCO^+ and e^- (lower panel). Models are distinguished by colors (Model 0: black; Model 6: magenta). Vertical dotted line marks the magneto-thermal wind bases for both models; vertical dash-dotted line indicates the EUV front.

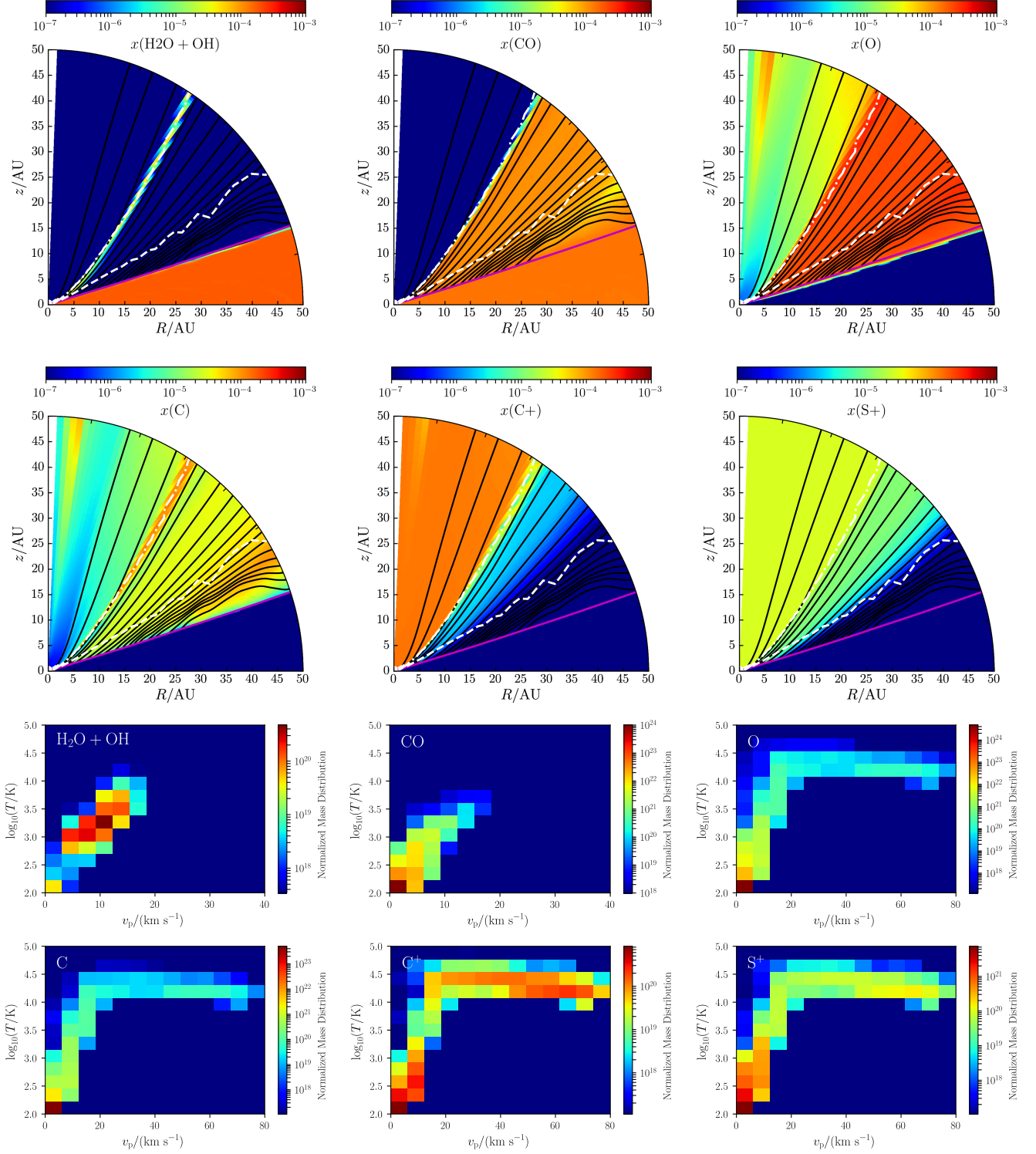


Figure 14. Like Figure 9 but for Model 6. White dash-dotted curves indicate the EUV front. Note that the ranges of temperature and velocity are different.

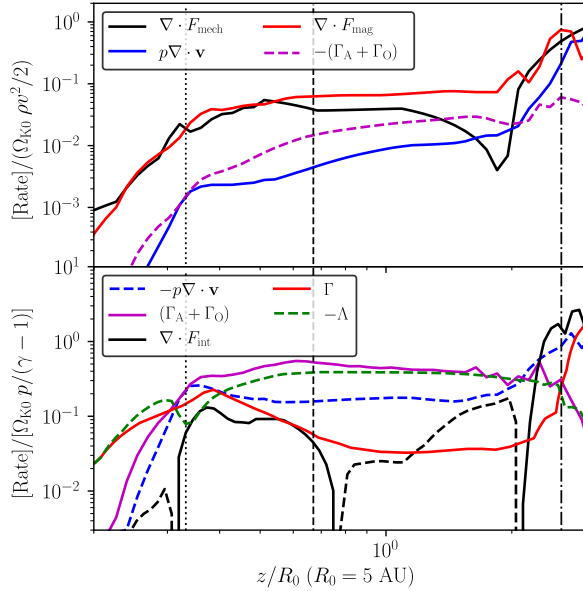


Figure 15. Like Figure 4 but for Model 6 and the field line anchored at $R_0 = 5$ au. Vertical dash-dotted lines indicate the EUV front.

and $\text{H}_2\text{O}/\text{OH}$ are similar to those of the fiducial model at the lower-left (low temperature, low v_p). The warm $\text{H}_2\text{O}/\text{OH}$ layer is found at lower altitudes than in the fiducial model; the conditions for re-formation of these molecules (see also §4.2.3) are satisfied in a thin layer dividing the magneto-thermal wind from the hot EUV wind. EUV ionization eliminates these molecules in the hot wind, where the temperature reaches $T \gtrsim 10^4$ K and the poloidal velocity $v_p \gtrsim 15$ km s $^{-1}$. Atomic species feature much higher velocities and temperatures than the molecules. Figure 14 shows that relatively significant amounts of neutral atomic O and C exist within the EUV hot wind layer and extend to similar temperatures and velocities as the ionized species. These relatively high-velocity tails in atomic species may be useful observationally to distinguish winds with EUV-driven components from purely magneto-thermal winds.

5.5. Disk Magnetization

Model 7 is distinguished from the fiducial model by stronger magnetization, i.e. ten times lower β_0 . The accretion rate is proportionately higher, but \dot{M}_{wind} is only ~ 6 times higher. The poloidal wind speed is slightly higher (~ 6.7 km s $^{-1}$), and the lever arm is larger, $R_a/R_{\text{wb}} \sim 1.5$ at all radii, yielding a smaller ejection index, $\xi \sim 0.5$. The mass density of the wind is larger, but not sufficient to prevent FUV and X-ray from reaching deeper than the Alfvénic surface. In contrast, B17 found the FUV front above the Alfvénic surface when β_0 increases to 10^4 . Toroidal motion in the wind is super-Keplerian in most places, but the net inertial (centrifugal

Table 6. Like Table 3 but for Model 6.

Species	\dot{M}	$\dot{M}/\dot{M}_{\text{wind}}$
	$(M_\odot \text{ yr}^{-1})$	
H_2	1.07×10^{-8}	6.11×10^{-1}
H	5.95×10^{-10}	3.41×10^{-2}
H^+	1.37×10^{-9}	7.83×10^{-2}
He	4.46×10^{-9}	2.56×10^{-1}
He^+	5.48×10^{-10}	3.15×10^{-2}
H_2O	6.15×10^{-15}	3.53×10^{-7}
OH	5.59×10^{-14}	3.21×10^{-6}
CO	2.84×10^{-11}	1.63×10^{-3}
O	4.14×10^{-11}	2.37×10^{-3}
O^+	6.75×10^{-12}	3.87×10^{-4}
C	6.30×10^{-12}	3.62×10^{-4}
C^+	2.55×10^{-12}	1.46×10^{-4}
S	8.41×10^{-12}	4.83×10^{-4}
S^+	2.82×10^{-12}	1.62×10^{-4}

gal plus gravitational) force projected onto field lines is still negative.

5.6. MHD Instability: the role of dust

Model 8 is rather special: it does not have a well-defined quasi-steady state; instead, it develops instabilities rather quickly, and these persist throughout the simulation.

Dust grains are crucial in the ionization balance of disks, especially near the midplane. In general, they assist recombination by adsorbing charged particles. If the dust abundance is reduced, regions with weaker magnetization become more ionized, which can make the system vulnerable to MRI. For Model 8, the MRI criterion (13) is satisfied in the accretion layer. This is illustrated in Figure 16, showing snapshots of β/β_{min} , magnetic stress, and field lines at $t = 60$ yr, when the instability is active. Thanks to increased Am, field lines in the accretion layer are better coupled to inward-moving gas, forming “spikes”. Within the unstable layer, $|T_{r\phi}^{\text{mag}}/(\rho v_r v_\phi)| \gtrsim 10$ (see also Figure 16). In contrast, for Model 0, this ratio is always smaller than unity. As axisymmetric 2.5-D simulations cannot deal with saturation of MRI properly, however, we choose not to over-interpret these results, and simply mark Model 8 “unstable”.

6. DISCUSSIONS

6.1. Comparison with B17

Although similar to B17 in many respects, by design, this work features the introduction of real-time consistent calculations of radiation and thermochemistry. How do these improvements modify the physical picture of the magneto-thermal wind mechanism?

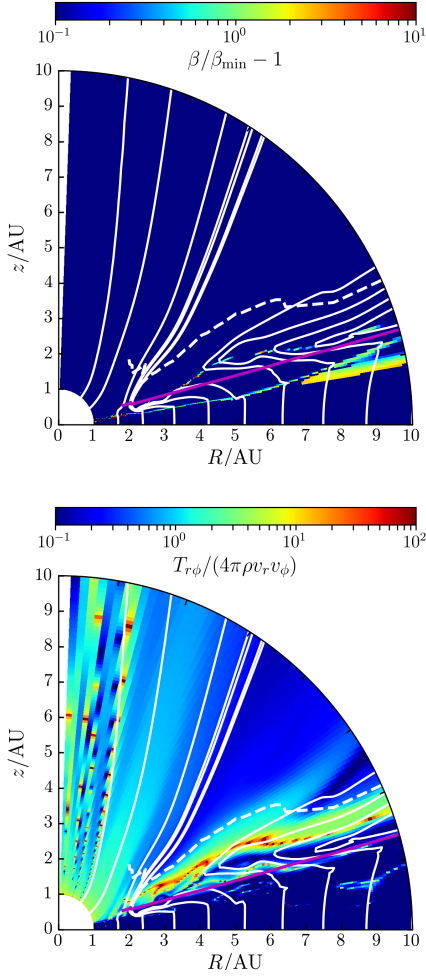


Figure 16. Meridional plots for Model 8 of $(\beta/\beta_{\min} - 1)$ (upper panel, see eq. 13) and $|T_{r\phi}^{\text{mag}}/(\rho v_r v_\phi)|$ (lower panel) showing a snapshot immediately after instabilities develop ($t \sim 60$ yr). Streamlines and field lines as in Figure 1.

The integrated mass-loss rate within the radial range $1 < R/\text{au} < 20$ is $2.1 \times 10^{-8} M_\odot \text{ yr}^{-1}$ versus B17’s $7.5 \times 10^{-8} M_\odot \text{ yr}^{-1}$. Yet the accretion rate throughout the same radial range is lower by no more than a factor of 1.5. Evidently, our winds have somewhat higher specific angular momentum (larger magnetic lever arm, smaller ejection index). The difference should mainly be attributed to our more consistent temperature and ionization structures. Near the wind base, the gas temperature and Am rise more sharply within the prescription of B17 than in this work (see Figures 2, 10). Shallower gradients can be expected to reduce \dot{M}_{wind} because the magnetic and thermal pressures reach the wind-launching threshold at somewhat lower gas density.

To better understand the difference in mass-loss rates and ejection indices between the present models and those of B17, we have compared their physical properties

in more detail. Figure 3 shows that the acceleration by gas pressure (f_{gas}) is greater than magnetic pressure (f_{mag}) at the wind base, and f_{gas} remains comparable to f_{mag} until the wind becomes super-Alfvénic. B17, in contrast, had f_{gas} making a much smaller or even negative contribution to wind launching. Another interesting comparison involves our Model 6 and the corresponding model with $\beta_0 \simeq 10^4$ in B17 (namely model B40). The latter features an FUV front above the Alfvénic surface; FUV photons are completely shielded from the acceleration region. Our Model 7, however, has FUV photons penetrating well below the Alfvén surface. Those deep-penetrating FUV photons are partially the reason that Model 6 has greater \dot{M}_{wind} than Model 0 by a factor of 6, while in B17 the corresponding factor is only 3. This difference emphasizes the value of consistent calculation of microphysics in non-ideal MHD simulations.

6.2. Comparison with WG17

Comparisons with WG17 are complicated by the different disk profile used here (and by B17). Nevertheless, it is significant that even before the poloidal magnetic field is applied, Model 6 exhibits $\dot{M}_{\text{wind}} \simeq 2.2 \times 10^{-9} M_\odot \text{ yr}^{-1}$ integrated over the range $1 < (r/\text{au}) < 50$ radial range, thanks to EUV radiation. This \dot{M}_{wind} is comparable to WG17’s fiducial result integrated over the range $2 < (r/\text{au}) < 100$.

Even after the field is applied and Model 5 reaches its magnetized steady state, there are major similarities to the unmagnetized models of WG17. In both cases, the vertical structure can be described as having three layers: (1) a relatively cold midplane that is shielded from high-energy radiation; (2) a warm ($T \sim 10^2 - 10^3$ K), largely molecular “intermediate layer”; and (3) a hot ($T \sim 10^4$ K), fast ($v_p \gtrsim 40 \text{ km s}^{-1}$) EUV-dominated wind. In fact, if we measure the mass flux only in the fast wind, we obtain a result ($2.6 \times 10^{-9} M_\odot \text{ yr}^{-1}$) very similar to that of the purely hydrodynamic simulations in WG17 ($2.5 \times 10^{-9} M_\odot \text{ yr}^{-1}$). The flow in the EUV-dominated wind is also similar to that in WG17, because gas pressure is comparable to magnetic pressure ($\beta \sim 10$; see Figure 11 and 12).

Nevertheless, including MHD drives the intermediate layer outwards via the magneto-thermal mechanism, in contrast to the radially static intermediate layers found by WG17. The mass-loss rate in the intermediate layer is approximately $1.6 \times 10^{-8} M_\odot \text{ yr}^{-1}$, and this gas is predominantly molecular. Therefore, we observe significant fraction of molecular species in the gas flowing out of the simulation domain (Table 6) in Model 6, while in WG17 molecules are depleted by photodissociation and photoionization before ever reaching the bound-

aries. Molecules are also found at higher velocities in these models than in those of WG17. For example, the distribution function of $\text{H}_2\text{O}/\text{OH}$ molecules extends to $\sim 15 \text{ km s}^{-1}$ (see Figure 14), compared to $\sim 10 \text{ km s}^{-1}$ in WG17’s figure 4. In addition, as toroidal fields provide more pressure, the outflowing “intermediate layer” is more inflated than that of WG17, which gives more the solid angle to intercept EUV photons and allows the fast wind to start with less depth of stellar gravitational potential. As a result, the EUV outflow has slightly higher velocity and density than WG17.

6.3. Implications for Observables

A major advantage of concurrently evolving a thermochemical network is that molecular/atomic signals are directly connected to the kinematics and dynamics of disk outflows, which holds out the promise that the underlying physics of PPD dispersal may be constrained by comparing these models with observations.

Another important possible goal is to distinguish PPD outflows driven by MHD effects from those driven solely by photoevaporation. WG17’s photoevaporative winds yield neutral atoms and molecules whose poloidal motion traces only the thin layer near the EUV wind bases base. These molecules dissociate before moving a significant distance within this layer, hence the toroidal motion of those molecules is almost Keplerian. Magneto-thermal winds, on the other hand, are substantially neutral and molecular. At high altitudes ($\theta \lesssim 0.6$), the neutral molecular winds deviate significantly and systematically from Keplerian. With ALMA data, Klaassen et al. (2013); Salyk et al. (2014); Bjerkeli et al. (2016) have already found significant large-scale molecular outflows. Optical and infrared observations on forbidden lines of atoms/ions (e.g. $[\text{O I}] \lambda 6300$) are also interpreted as signatures of PPD winds (e.g. Hartigan et al. 1995; Natta et al. 2014; Simon et al. 2016; Fang et al. 2018; Banzatti et al. 2018, submitted). In addition, Flaherty et al. (2018) constrained the amplitude of turbulence inside the disk of TW Hya and concluded that $\alpha < 0.007$. These result may constrain the wind-launching and accretion mechanisms by comparing with models, such as ours, that predict the kinematics and dynamics of the observed species.

7. SUMMARY

We have studied PPD outflows by conducting axisymmetric global simulations that combine non-ideal MHD (excepting the Hall effect) with consistent ray-tracing radiative transfer and thermochemistry. Our fiducial model, whose parameters broadly follow B17, features a warm ($T \sim 10^2\text{-}10^3 \text{ K}$), predominantly molecular, magneto-thermal wind, driven by the gradient of

toroidal magnetic pressure. Such wind has mostly sub-Keplerian toroidal motion, with typical radial velocity $\lesssim 5 \text{ km s}^{-1}$ and a mass-loss rate comparable to the magnetically driven accretion rate. By varying luminosities of high energy photons, especially soft-FUV and Lyman-Werner photons, we find that the wind mass loss is affected by the ionization fraction and ambipolar parameter near the wind base, though, overall rates of mass-loss and accretion are relatively robust against variations in luminosities. Adding EUV photons adds a fast ($v_p \gtrsim 50 \text{ km s}^{-1}$), hot ($T \gtrsim 10^4 \text{ K}$), ionized component to the wind at high latitudes. For plausible EUV luminosities, the pressure of the fast atomic wind compresses the latitudinal range of the molecular wind and reduces its mass-loss rate by about a half. Reducing the dust abundance may raise the ionization fraction near the wind base, leading to MRI-like instabilities. This illustrates that the structure and dynamics of magneto-thermal winds may well depend sensitively on subtle details of thermochemistry.

In the future we expect to explore several other aspects of problems as natural extensions to this work. Adding Hall effect will likely substantially change the flow structure and magnetic flux transport in the disk, affecting wind launching (Bai & Stone 2017, B17). Because B17 found that the Hall effect tends to break the reflection symmetry about the midplane, this in turn may require better treatment of midplane thermochemistry. Adsorption and desorption of volatile species on surfaces of dust grains, processes that we have so far neglected, may change the thermochemical conditions at the wind base, and in turn affect the wind dynamics. Monte-Carlo modeling of scattered/re-emitted photons (especially infrared and X-ray photons), instead of simplified recipes, may be needed. Some parts of the parameter space show signs of MRI instabilities, which should properly be studied by 3-dimensional global simulations. In fact, even the laminar models may be subject to 3D kink instabilities in regions where $B_\phi/B_p \gg 1$. Modeling the molecular and atomic lines implied by these simulations will help us to better constrain our models by comparison to observations and improve our understanding of the dispersal and accretion of PPDs.

This work was supported by NASA under grant 17-ATP17-0094/80NSSC18K0567 and by Princeton University’s Department of Astrophysical Sciences. We thank our colleagues: Phil Armitage, Bruce Draine, Eve Ostriker, James Stone, and Kengo Tomida, for discussions and for detailed comments on preliminary versions

of this paper. We also thank Oliver Gressel who inspired the explorations in non-ideal MHD heating in this work.

APPENDIX

A. ADDITIONAL DETAILS OF RADIATION AND THERMOCHEMICAL PROCESSES

This appendix provides details concerning the treatment of some thermochemical and radiation processes, especially treatments that have been improved since WG17.

A.1. Ionization by Diffuse High Energy Photons and Radioactive Decay

We follow the recipes in [Bai & Goodman \(2009\)](#). The effective ionization rate by diffuse sources of ionization is

$$\xi^{\text{eff}} = \xi_{\text{X-ray}}^{\text{eff}} + \xi_{\text{CR}}^{\text{eff}} + \xi_{\text{SLR}}^{\text{eff}} . \quad (\text{A1})$$

The term $\xi_{\text{X-ray}}^{\text{eff}}$ represents ionization by down-scattered X-ray photons and is approximated by a fitting formula based on [Igea & Glassgold \(1999\)](#),

$$\xi_{\text{X-ray}}^{\text{eff}} = \left(\frac{R}{\text{au}} \right)^{-2.2} \left(\frac{L_{\text{X}}}{10^{29} \text{ erg s}^{-1}} \right)^2 \left\{ \xi_1 \left[e^{-(N_{\text{H1}}/N_1)^\alpha} + e^{-(N_{\text{H2}}/N_1)^\alpha} \right] + \xi_2 \left[e^{-(N_{\text{H1}}/N_2)^\beta} + e^{-(N_{\text{H2}}/N_2)^\beta} \right] \right\} . \quad (\text{A2})$$

Here L_{X} is the X-ray luminosity (in our simulations, the luminosity in the 3 keV energy band). The terms involving ξ_1 and ξ_2 describe attenuation by absorption and scattering, respectively, while N_{H1} and N_{H2} are the vertical column densities of hydrogen nuclei measured above and below the point of interest (thus accounting for penetration from both sides of the disk). $\xi_1 = 4.0 \times 10^{-12} \text{ s}^{-1}$, $\xi_2 = 2.0 \times 10^{-15} \text{ s}^{-1}$, $N_1 = 1.5 \times 10^{21} \text{ cm}^{-2}$, $N_2 = 7.0 \times 10^{23} \text{ cm}^{-2}$, $\alpha = 0.5$, and $\beta = 0.65$. For the sake of simplicity we approximate the vertical density profile as Gaussian and take,

$$\begin{aligned} N_{\text{H1}}(z) &= n_{\text{H}}(z) \int_z^{+\infty} dz' e^{(z^2 - z'^2)/2h^2} \sim h n_{\text{H}}(z) , \\ N_{\text{H2}}(z) &= n_{\text{H}}(z) \int_{-\infty}^{+\infty} dz' e^{(z^2 - z'^2)/2h^2} - N_{\text{H1}}(z) \sim 2.5h e^{z^2/2h^2} n_{\text{H}}(z) - N_{\text{H1}}(z) , \end{aligned} \quad (\text{A3})$$

where $h \equiv c_s/\Omega$ is the local disk scale height based on the midplane isothermal sound speed c_s , and n_{H} is the local number density of hydrogen nuclei. Rough estimates as eqs. (A3) are, we verify for each model that such estimates are different from exact results by no more than $\sim 20\%$ near and below the wind base.

The cosmic ray term, $\xi_{\text{CR}}^{\text{eff}}$, is approximated using the updated recipes in [Umebayashi & Nakano \(1981\)](#)

$$\xi_{\text{CR}}^{\text{eff}} = 10^{-17} \text{ s}^{-1} \times \left(e^{-N_{\text{H1}}/N_{\text{CR}}} + e^{-N_{\text{H2}}/N_{\text{CR}}} \right) , \quad (\text{A4})$$

where $N_{\text{CR}} = 5.7 \times 10^{25} \text{ cm}^{-2}$. The contribution of short-lived radioactive nuclei is presumed constant, $\xi_{\text{SLR}}^{\text{eff}} = 6.0 \times 10^{-19} \text{ s}^{-1}$. The effective ionization rate is divided among three channels according to

$$\begin{aligned} \text{H}_2 &\rightarrow \text{H} + \text{H}^+ + e^- , \quad \xi = \xi^{\text{eff}} ; \\ \text{H} &\rightarrow \text{H}^+ + e^- , \quad \xi = 0.50 \xi^{\text{eff}} ; \\ \text{He} &\rightarrow \text{He}^+ + e^- , \quad \xi = 0.84 \xi^{\text{eff}} ; \end{aligned} \quad (\text{A5})$$

Admittedly these are rather rough estimates. However, the focus of this paper is on the disk atmosphere and wind zone, where the X-rays are scarcely attenuated and the other sources of ionization above—cosmic rays and radioactivities—are less important.

A.2. Self-/Cross-Shielding and Absorption of FUV Photons

Some photoreactions, especially photoionizations and photodissociations by absorption lines (e.g. in the LW band), are subject to self-/cross-shielding effects. For the dominant species in the intermediate zone, H_2 , we adopt the scheme in WG17, which treats the photo-pumping $\text{H}_2 + h\nu(\text{LW}) \rightarrow \text{H}_2^*$ with the self-shielding recipes in [Draine & Bertoldi \(1996\)](#). Such photo-pumping is the starting point of some important subsequent processes, including collisional heating, dissociation, and spontaneous decay. For other species, we adopt the tabulated self-shielding and cross-shielding coefficients (by H_2 and by C if applicable) obtained by [Heays et al. \(2017\)](#) for the photoreactions of the following species: C, CO, S, Si, and SiO.

A.3. Pre-absorption of Radiation at the Inner Radial Boundary

As our simulations exclude the central zone, ionizing radiation is not attenuated by any outflow or raised disk rim at $r < r_{\text{in}}$. At low latitudes in the predominantly neutral outflow near the inner radial boundary, this absence of attenuation could cause unphysically high ionization fractions, which compromise the credibility and even stability of our simulations. We therefore use a “pre-absorption” scheme to account for such attenuation: for each energy bin, the absorption optical depth of a ray at co-latitude θ from the central source to the inner boundary r_{in} , $\tau_{\text{in}}(h\nu, \theta)$, is estimated as follows. We assume that the ratio $\tau_{\text{out}}(h\nu, \theta)/\tau_{\text{in}}(h\nu, \theta)$ equals $\zeta^{-1}r_{\text{in}}/r_{\text{out}}$, where ζ is a constant factor, and $(\tau_{\text{out}}(h\nu, \theta))$ is the absorption optical depth between r_{in} and r_{out} along the same ray. Hence,

$$\tau_{\text{in}}(h\nu, \theta) \simeq \zeta \frac{r_{\text{in}}}{r_{\text{out}}} \tau_{\text{out}}(h\nu, \theta) ; \quad \tau_{\text{out}}(h\nu, \theta) = \ln \left[\frac{F_{\text{in}}(h\nu, \theta)}{F_{\text{out}}(h\nu, \theta)} \right] , \quad (\text{A6})$$

where $F_{\text{in}}(h\nu, \theta)$ and $F_{\text{out}}(h\nu, \theta)$ are the photon fluxes along the ray at the inner and outer boundaries, respectively. F_{in} and F_{out} are measured from the previous time step. We tested several values of ζ from 10^{-1} to 10^1 , confirming that the results of simulations are not sensitive to ζ . For convenience we choose $\zeta = 1$ throughout this work.

REFERENCES

- Ádámkóvics, M., Glassgold, A. E., & Najita, J. R. 2014, *ApJ*, 786, 135
- Alexander, R. D., Clarke, C. J., & Pringle, J. E. 2006a, *MNRAS*, 369, 216
- . 2006b, *MNRAS*, 369, 229
- Bai, X.-N. 2011a, *ApJ*, 739, 50
- . 2011b, *ApJ*, 739, 51
- . 2013, *ApJ*, 772, 96
- . 2016, *ApJ*, 821, 80
- . 2017, *ApJ*, 845, 75, (B17)
- Bai, X.-N., & Goodman, J. 2009, *ApJ*, 701, 737
- Bai, X.-N., & Stone, J. M. 2011, *ApJ*, 736, 144
- . 2013, *ApJ*, 769, 76
- . 2017, *ApJ*, 836, 46
- Bai, X.-N., Ye, J., Goodman, J., & Yuan, F. 2016, *ApJ*, 818, 152
- Balbus, S. A., & Hawley, J. F. 1998, *Reviews of Modern Physics*, 70, 1
- Bethell, T. J., & Bergin, E. A. 2011, *ApJ*, 739, 78
- Bjerkeli, P., van der Wiel, M. H. D., Harsono, D., Ramsey, J. P., & Jørgensen, J. K. 2016, *Nature*, 540, 406
- Chiang, E. I., & Goldreich, P. 1997, *ApJ*, 490, 368
- Draine, B. T. 2011, *Physics of the Interstellar and Intergalactic Medium* (Princeton University Press)
- Draine, B. T., & Bertoldi, F. 1996, *ApJ*, 468, 269
- Draine, B. T., & Sutin, B. 1987, *ApJ*, 320, 803
- Fang, M., Pascucci, I., Edwards, S., et al. 2018, *ArXiv e-prints*, arXiv:1810.03366
- Ferreira, J., & Pelletier, G. 1995, *A&A*, 295, 807
- Flaherty, K. M., Hughes, A. M., Teague, R., et al. 2018, *ApJ*, 856, 117
- Garcia, P. J. V., Ferreira, J., Cabrit, S., & Binette, L. 2001, *A&A*, 377, 589
- Geers, V. C., Augereau, J.-C., Pontoppidan, K. M., et al. 2006, *A&A*, 459, 545
- Goldsmith, P. F. 2001, *ApJ*, 557, 736
- Gorti, U., & Hollenbach, D. 2008, *ApJ*, 683, 287
- . 2009, *ApJ*, 690, 1539
- Gressel, O., Turner, N. J., Nelson, R. P., & McNally, C. P. 2015, *ApJ*, 801, 84
- Hartigan, P., Edwards, S., & Ghandour, L. 1995, *ApJ*, 452, 736
- Heays, A. N., Bosman, A. D., & van Dishoeck, E. F. 2017, *A&A*, 602, A105
- Igea, J., & Glassgold, A. E. 1999, *ApJ*, 518, 848
- Ilgner, M., & Nelson, R. P. 2006, *A&A*, 445, 205
- . 2008, *A&A*, 483, 815
- Jenkins, E. B. 2009, *ApJ*, 700, 1299
- Klaassen, P. D., Juhasz, A., Mathews, G. S., et al. 2013, *A&A*, 555, A73
- Kwan, J., & Krolik, J. H. 1981, *ApJ*, 250, 478
- Li, A., & Draine, B. T. 2001, *ApJ*, 554, 778
- McElroy, D., Walsh, C., Markwick, A. J., et al. 2013, *A&A*, 550, A36
- Nakatani, R., Hosokawa, T., Yoshida, N., Nomura, H., & Kuiper, R. 2018, *ApJ*, 857, 57
- Natta, A., Testi, L., Alcalá, J. M., et al. 2014, *A&A*, 569, A5
- Nelson, R. P., Gressel, O., & Umurhan, O. M. 2013, *MNRAS*, 435, 2610
- Neufeld, D. A., & Kaufman, M. J. 1993, *ApJ*, 418, 263
- Omukai, K., Hosokawa, T., & Yoshida, N. 2010, *ApJ*, 722, 1793
- Owen, J. E., Ercolano, B., Clarke, C. J., & Alexander, R. D. 2010, *MNRAS*, 401, 1415
- Safier, P. N. 1993, *ApJ*, 408, 115

- Salyk, C., Pontoppidan, K., Corder, S., et al. 2014, *ApJ*, 792, 68
- Shakura, N. I., & Sunyaev, R. A. 1973, *A&A*, 24, 337
- Simon, J. B., Bai, X.-N., Armitage, P. J., Stone, J. M., & Beckwith, K. 2013a, *ApJ*, 775, 73
- Simon, J. B., Bai, X.-N., Stone, J. M., Armitage, P. J., & Beckwith, K. 2013b, *ApJ*, 764, 66
- Simon, M. N., Pascucci, I., Edwards, S., et al. 2016, *ApJ*, 831, 169
- Tielens, A. G. G. M. 2008, *ARA&A*, 46, 289
- Tielens, A. G. G. M., & Hollenbach, D. 1985, *ApJ*, 291, 722
- Turner, N. J., Fromang, S., Gammie, C., et al. 2014, *Protostars and Planets VI*, 411
- Turner, N. J., Sano, T., & Dziourkevitch, N. 2007, *ApJ*, 659, 729
- Umebayashi, T., & Nakano, T. 1981, *PASJ*, 33, 617
- Verner, D. A., Ferland, G. J., Korista, K. T., & Yakovlev, D. G. 1996, *ApJ*, 465, 487
- Verner, D. A., & Yakovlev, D. G. 1995, *A&AS*, 109
- Visser, R., van Dishoeck, E. F., & Black, J. H. 2009, *A&A*, 503, 323
- Wang, L., & Goodman, J. 2017a, *ApJ*, 847, 11, (**WG17**)
- . 2017b, *ApJ*, 835, 59
- Wardle, M. 2007, *Ap&SS*, 311, 35
- Weingartner, J. C., & Draine, B. T. 2001, *ApJS*, 134, 263
- White, C. J., Stone, J. M., & Gammie, C. F. 2016, *ApJS*, 225, 22
- Woitke, P., Min, M., Pinte, C., et al. 2016, *A&A*, 586, A103
- Xu, R., & Bai, X.-N. 2016, *ApJ*, 819, 68
- Zanni, C., Ferrari, A., Rosner, R., Bodo, G., & Massaglia, S. 2007, *A&A*, 469, 811